

# Hofstadter Physics and Composite Fermionic Phase in Moiré Systems

by

Shuhan Ding

B.S. Applied Physics, University of Science and Technology of China, 2022

Submitted to the Department of Nuclear Science and Engineering  
in partial fulfillment of the requirements for the degree of

MASTER OF SCIENCE IN NUCLEAR SCIENCE AND ENGINEERING

at the

MASSACHUSETTS INSTITUTE OF TECHNOLOGY

September 2024

© 2024 Shuhan Ding. This work is licensed under a [CC BY-NC-ND 4.0](#) license.

The author hereby grants to MIT a nonexclusive, worldwide, irrevocable, royalty-free  
license to exercise any and all rights under copyright, including to reproduce, preserve,  
distribute and publicly display copies of the thesis, or release the thesis under an  
open-access license.

Authored by: Shuhan Ding  
Department of Nuclear Science and Engineering  
August 26, 2024

Certified by: Ju Li  
Department of Nuclear Science and Engineering  
Thesis Supervisor

Accepted by: Ju Li  
Department of Nuclear Science and Engineering  
Chair, Department Committee on Graduate Students



# Hofstadter Physics and Composite Fermionic Phase in Moiré Systems

by

Shuhan Ding

Submitted to the Department of Nuclear Science and Engineering  
on August 26, 2024 in partial fulfillment of the requirements for the degree of

MASTER OF SCIENCE IN NUCLEAR SCIENCE AND ENGINEERING

## ABSTRACT

This thesis explores the intricate electronic phenomena in Moiré systems, particularly focusing on twisted bilayer transition metal dichalcogenides (TMD). These systems, with their unique superlattice structures and strong electron correlations, provide fertile ground for investigating novel quantum states. A key focus is on understanding Hofstadter physics and the emergence of composite fermion phases in these materials.

In this work, we first develop a continuum model to describe the low-energy electronic structure of twisted TMD bilayers, emphasizing the role of the Moiré superlattice in modifying the band structure and introducing non-trivial topological properties. We analyze the resulting Hofstadter spectrum under an external magnetic field, revealing the rich fractal pattern and the impact of valley polarization induced by the magnetic field.

Building on this framework, we delve into the concept of composite fermions, particularly in the context of the fractional quantum Hall effect (FQHE). We extend Jain's composite fermion theory and the Chern-Simons field theory to Moiré TMD systems, proposing the existence of an anomalous composite fermion liquid state at half-filling. Through a detailed mean-field analysis, we demonstrate that this state, characterized by a strong valley polar-

ization and an effective magnetic field arising from Berry curvature, could be energetically favored under certain conditions.

Our findings suggest that Moiré TMDs are promising candidates for realizing fractional Chern insulators and other exotic quantum phases, opening up new avenues for experimental exploration and potential applications in quantum technology.

Thesis supervisor: Ju Li

Title: Tokyo Electric Power Company Professor in Nuclear Engineering

# Acknowledgments

I would like to express my deepest gratitude to my advisor, Professor Ju Li, whose expertise, patience, and guidance have been instrumental in the successful completion of this thesis. His insights and feedback have helped me navigate the complexities of my research, and his unwavering support has motivated me throughout this journey.

I am also grateful to my former professor, Liang Fu. His insightful ideas and guidance provided valuable direction to my research, and I learned a great deal from our discussions.

I want to extend my heartfelt thanks to Professor Yao Wang, who has been a tremendous help throughout my academic life. Her support and encouragement have been invaluable to my growth as a researcher. I am also very thankful to Professor Mingda Li for his constant support and encouragement during my time at MIT.

I would like to express my sincere appreciation to Brandy Baker and the other administrative staff in the department, who provided me with warm and thoughtful assistance. Their kindness and support have made my experience at MIT all the more meaningful.

On a personal note, I owe my deepest thanks to my family for their unconditional love, patience, and encouragement. To my parents, Li Yang and Hongge Ding, thank you for always believing in me and supporting my academic pursuits. To my girlfriend, Ziyuan Yang, your constant support and understanding have been my anchor throughout this journey.

Lastly, I would like to thank everyone who has supported me, directly or indirectly, throughout my academic career. Your encouragement and belief in my potential have been invaluable to my success.



# Contents

<b>Title page</b>	<b>1</b>
<b>Abstract</b>	<b>3</b>
<b>Acknowledgments</b>	<b>5</b>
<b>List of Figures</b>	<b>9</b>
<b>List of Tables</b>	<b>11</b>
<b>1 Introduction</b>	<b>13</b>
1.1 The Two-Dimensional Moiré System . . . . .	13
1.2 Quantum Hall Effect . . . . .	14
1.3 Outline of the Thesis . . . . .	14
<b>2 Electron in Periodic Potential with Homogeneous Magnetic Field</b>	<b>17</b>
2.1 Landau Level . . . . .	18
2.2 Generalized Bloch Conditions . . . . .	21
2.3 Fractional Coordinates . . . . .	24
2.4 Numerical Methods . . . . .	25
2.4.1 Plane-wave-based algorithms . . . . .	25
2.4.2 Conjugate gradient method . . . . .	28
2.4.3 Relaxation Method . . . . .	32

<b>3 Hofstadter Physics of Moiré Transition Metal Dichalcogenides</b>	<b>37</b>
3.1 Introduction . . . . .	37
3.2 Continuum Model of TMD . . . . .	39
3.3 Hofstadter Spectrum in Moiré TMD . . . . .	44
3.4 Quantum Hall conductivity and Wannier's diagrams . . . . .	47
3.5 Conclusion . . . . .	50
<b>4 Composite Fermions Mean-field Theory for Moiré Transition Metal Dichalcogenides</b>	<b>53</b>
4.1 Introduction . . . . .	53
4.2 Theoretical Framework . . . . .	55
4.2.1 Jain's Composite Fermion Theory . . . . .	55
4.2.2 Chern-Simons Field Theory and Flux Attachment . . . . .	56
4.2.3 Composite Fermion Liquid Theory . . . . .	57
4.2.4 Application to Moiré TMD Systems . . . . .	57
4.3 Composite Fermion Mean-field Theory in TMD . . . . .	58
4.4 Mean-field Evidence for Anomalous Composite Fermion Liquid State . . . . .	62
4.5 Discussion . . . . .	65
<b>5 Conclusions and Future Work</b>	<b>67</b>
5.1 Conclusions . . . . .	67
5.2 Future Work . . . . .	68
<b>References</b>	<b>71</b>

# List of Figures

3.1 Moiré band structure of twisted MoTe <sub>2</sub> homobilayer with twist angle (a) $\theta = 1.2^\circ$ , (b) $\theta = 2.0^\circ$ , and (c) $\theta = 3.0^\circ$ . The Chern numbers $C$ of each band is labeled in valley $K$ , while $C$ should change sign in valley $K'$ due to the time-reversal symmetry. . . . .	43
3.2 Berry curvatures of the lowest energy band for a MoTe <sub>2</sub> homobilayer at the $K$ valley, with twist angles: (a) $\theta = 1.2^\circ$ , (b) $\theta = 2.0^\circ$ , and (c) $\theta = 3.0^\circ$ . The Berry curvature exhibits a sign change at the $K'$ valley. The calculated Chern numbers for all three twist angles are $C = -1$ , which would also reverse sign at the $K'$ valley. . . . .	44
3.3 Hofstadter spectra of a MoTe <sub>2</sub> homobilayer with twist angles: (a) $\theta = 1.2^\circ$ , (c) $\theta = 2.0^\circ$ , and (d) $\theta = 3.0^\circ$ . Panel (b) shows a zoom-in of the spectrum in (a) at $\theta = 1.2^\circ$ . For comparison, the Hofstadter spectra of the nearest-neighbor tight-binding model on (e) a honeycomb lattice and (f) a triangular lattice are also presented. . . . .	46
3.4 Hall conductivity of MoTe <sub>2</sub> homobilayer with twist angle (a)(b) $\theta = 1.2^\circ$ , (c) $\theta = 2.0^\circ$ , and (d) $\theta = 3.0^\circ$ , where (b) is a zoom-in of (a). . . . .	48

3.5 Wannier diagrams showing the energy density of states (DOS) for a MoTe <sub>2</sub> homobilayer at different twist angles: (a) $\theta = 1.2^\circ$ , (b) $\theta = 2.0^\circ$ , and (c) $\theta = 3.0^\circ$ . The x-axis represents the magnetic flux per Moiré unit cell, while the y-axis indicates the filling factor, corresponding to the number of electrons per Moiré unit cell. . . . .	50
4.1 SCF sultions of twisted MoTe <sub>2</sub> homobilayer with twist angle $\theta = 2.0^\circ$ at half-filling with $2\Phi_0$ flux attachment per electron, where (a) is the charge density $n(\mathbf{r})$ , (b) is $B_{\text{var}}(\mathbf{r})$ , and (c) is $\mathbf{A}_{\text{var}}(\mathbf{r})$ . The upper (lower) figures is calculated in valley $K$ ( $K'$ ). . . . .	61
4.2 Mean-field band structures of a twisted MoTe <sub>2</sub> homobilayer at twist angles: (a) $\theta = 1.2^\circ$ , (b) $\theta = 2.0^\circ$ , and (c) $\theta = 3.0^\circ$ . The blue and red lines represent composite fermions with a flux attachment of $2\Phi_0$ per electron in valleys $K$ and $K'$ , respectively, while the gray dashed lines indicate the band structures of bare electrons without flux attachment in either valley. Panels (d) and (e) provide a comparison to the free-particle limit (green lines) for valleys $K$ at twist angles $\theta = 2.0^\circ$ and $\theta = 3.0^\circ$ , respectively. . . . .	63

## List of Tables



# Chapter 1

## Introduction

### 1.1 The Two-Dimensional Moiré System

Two-dimensional (2D) materials, such as graphene and transition metal dichalcogenides (TMD), have become a focal point in condensed matter physics due to their extraordinary electronic properties. When two layers of these materials are stacked with a small twist angle or slight lattice mismatch, they form a Moiré pattern—a superlattice that significantly alters the electronic characteristics of the system [1]. This new periodic potential introduces an energy scale much smaller than that of the original atomic lattice, allowing researchers to explore electronic phenomena at lower energy scales. The resulting flattening of electronic bands enhances electron-electron interactions, providing fertile ground for studying correlated electronic states such as superconductivity, Mott insulators, and other exotic quantum phases [2]–[7]. Moreover, the twist angle between layers offers an additional degree of control over these interactions, making Moiré systems a versatile platform for investigating novel quantum states of matter.

The study of Moiré systems has revealed new quantum phenomena, including the emergence of topologically protected states, Hofstadter physics at accessible magnetic fields [8]–[10], and the potential realization of fractional Chern insulators (FCI) [5]–[7]. These find-

ings have profound implications for the development of quantum materials and technologies, including quantum computing and high-precision metrology.

## 1.2 Quantum Hall Effect

The quantum Hall effect (QHE) is one of the most striking phenomena in condensed matter physics, characterized by the quantization of Hall conductance in two-dimensional electron systems under a strong perpendicular magnetic field [11]. The integer quantum Hall effect (IQHE) and the fractional quantum Hall effect (FQHE) have provided deep insights into electron interactions and topological phases of matter.

The IQHE, with Hall conductance quantized in integer multiples of the elementary quantum  $e^2/h$ , arises from the formation of discrete Landau levels in a magnetic field, and can be understood within the framework of non-interacting electrons [12].

The FQHE, occurring at fractional filling factors, represents a fundamentally different phenomenon, driven by strong electron-electron interactions. It can be understood through the composite fermion theory proposed by Jainendra Jain [13], which elegantly maps the FQHE to an integer quantum Hall effect of composite fermions—quasiparticles formed by attaching an even number of magnetic flux quanta to electrons. This theory has greatly expanded our understanding of quantum Hall effects, and its relevance has extended to Moiré systems, where the interplay between superlattice potentials and magnetic fields leads to new manifestations of the QHE, such as the Hofstadter butterfly [14] and fractional Chern insulators [15].

## 1.3 Outline of the Thesis

This thesis is organized to explore the electronic structure in Moiré systems with external or intrinsic magnetic fields, with a particular focus on twisted bilayer TMD. The study begins in chapter 2, where we discuss the electronic structure of materials subjected to both a periodic

potential and an external uniform magnetic field, emphasizing the formation of Landau levels and the application of generalized Bloch conditions, and develop numerical algorithms to simulate the systems. In chapter. 3, we delve into the Hofstadter physics of twisted bilayer TMD, deriving the continuum model for these systems and analyzing the resulting Hofstadter spectrum. The chapter also discusses how these findings relate to quantum Hall conductivity and the potential for observing quantum Hall states by experiments. Chapter. 4 focuses on the concept of composite fermions, introducing composite fermion theory and applying it to Moiré TMD systems. It presents a detailed mean-field analysis to argue for the existence of an anomalous composite fermion liquid state at half-filling in these systems. This chapter demonstrates that such a state, characterized by a strong valley polarization and an effective magnetic field arising from the Berry curvature, could be energetically favored under certain conditions. The implications of this for the realization of fractional Chern insulators (FCI) are also explored. Chapter. 5 concludes the thesis by summarizing the key findings and highlighting the potential avenues for future research. This includes the experimental validation of the predicted quantum phases, the exploration of interaction effects beyond mean-field theory, and the extension of Moiré physics studies to other 2D materials.



# Chapter 2

## Electron in Periodic Potential with Homogeneous Magnetic Field

Understanding the electronic structure of materials is a fundamental aspect of condensed matter physics, providing critical insights into their electrical, magnetic, and optical properties. When electrons move in a crystal lattice, they experience a periodic potential due to the arrangement of atoms. This periodic potential significantly influences their behavior, giving rise to phenomena such as band structures and electronic band gaps. Additionally, the presence of an external uniform magnetic field further complicates the scenario by introducing Lorentz forces that modify the electron trajectories, leading to quantized cyclotron orbits and the formation of Landau levels.

The interplay between the periodic potential of a crystal lattice and an external magnetic field is particularly fascinating and complex. It gives rise to a rich variety of physical phenomena, including the quantum Hall effect, magnetic breakdown, and the emergence of novel quasiparticles like magnetic polarons and composite fermions. To accurately describe and predict these phenomena, advanced computational algorithms are indispensable.

Computational methods for studying electronic structures under these conditions must address several challenges. They need to account for the periodic potential of the crystal lat-

tice, the influence of the magnetic field, and the interactions between electrons. Traditional methods, such as tight-binding models and nearly free electron approximations, often serve as the starting point. However, these methods are limited to certain scenarios where their approximations are valid, and an unbiased treatment of the regimes where these approximations fail is desirable.

Moreover, modern computational approaches leverage numerical techniques and high-performance computing to solve the Schrödinger equation for electrons in these complex environments. Methods such as density functional theory (DFT) and Hartree-Fock approximations have been adapted to incorporate magnetic fields. Additionally, specialized algorithms, including the Landau-level-based method and plane-wave based method, have been developed to handle the unique challenges posed by magnetic fields.

This chapter aims to provide a comprehensive overview of the computational algorithms used to investigate the electronic structure of materials subjected to a periodic potential and an external uniform magnetic field. We will explore the theoretical foundations of these methods, discuss their implementation, and highlight their applications in understanding and predicting material properties. We will first discuss the behavior of electrons in a uniform magnetic field and in a periodic potential, respectively. Then we will discuss the behavior of electrons in the presence of both. Finally, we will summarize and compare algorithms for calculating the electronic structure in such cases, and delve deeper into plane-wave based algorithm.

## 2.1 Landau Level

The concept of Landau levels was introduced by Lev Landau [16] in 1930 as part of his investigation into the quantum mechanics of charged particles in magnetic fields. In his seminal paper, Landau employed the Schrödinger equation to show that an electron confined to a plane and subjected to a perpendicular magnetic field exhibits quantized energy levels,

now known as Landau levels. This theoretical breakthrough provided a deeper understanding of how magnetic fields influence quantum systems and laid the groundwork for future research in quantum mechanics and condensed matter physics.

To understand the quantization of Landau levels, we start by considering the Hamiltonian for a charged particle, such as an electron, moving in a two-dimensional plane under a uniform perpendicular magnetic field  $\mathbf{B} = B\hat{\mathbf{z}}$ . The vector potential  $\mathbf{A}$  can be chosen such that  $\mathbf{B} = \nabla \times \mathbf{A}$ .

The Hamiltonian of the system is given by

$$H_{\text{LL}} = \frac{1}{2m}(\mathbf{p} + e\mathbf{A})^2, \quad (2.1)$$

where  $m$  is the mass of the electron,  $-e$  is the charge of the electron, and  $\mathbf{p}$  is the canonical momentum. There are different choices for the vector potential  $A$  that can simplify the calculations. Two common choices are

- Landau Gauge:  $\mathbf{A} = B\hat{\mathbf{y}}\hat{\mathbf{x}} \cdot \mathbf{r} = B(0, x, 0)$

This gauge preserves the translational symmetry in the y- and z- directions but breaks the rotational symmetry and the translational symmetry in the x-direction.

- Symmetric Gauge:  $\mathbf{A} = \frac{1}{2}\mathbf{B} \times \mathbf{r} = \frac{1}{2}B(y, x, 0)$

This gauge preserves the rotational symmetry and the translational symmetry in z-direction but breaks the translational symmetries in both x- and y- directions.

Each gauge leads to different forms of the Hamiltonian but ultimately yields the same physics.

In following section, We consider the Landau gauge  $\mathbf{A} = B(0, x, 0)$ . The choice of this gauge is consistent with the magnetic translational symmetry that will be illustrated later. The corresponding Hamiltonian is

$$H_{\text{LL}} = \frac{p_x^2}{2m} + \frac{1}{2m}(p_y + eBx)^2 + \frac{p_z^2}{2m}. \quad (2.2)$$

Since the Hamiltonian preserves momentum in y- and z- directions, the eigen wave-function can be separated into  $\psi(\mathbf{r}) = e^{i(k_y y + k_z z)} \phi(x)$ , and the representation of  $H$  under this basis is

$$H_{\text{LL}} = -\frac{\hbar^2}{2m} \partial_x^2 + \frac{1}{2} m \omega_c^2 \left( x + \frac{\hbar k_y}{m \omega_c} \right)^2 + \frac{\hbar^2 k_z^2}{2m} \quad (2.3)$$

where  $\omega_c = eB/m$  is the cyclotron frequency. The Hamiltonian displays a simple harmonic oscillator (SHO) behavior in the x-direction but with a shift of the guiding center position  $x_c = -\frac{\hbar k_y}{m \omega_c}$  proportional to  $k_y$ . From this observation, the eigen wave-functions is a direct product of the plane-wave and SHO wavefunction

$$\psi(\mathbf{r}) = e^{i(k_y y + k_z z)} \phi_n \left( x - x_c(k_y) \right) \quad (2.4)$$

with  $n \geq 0$  an integer denoting the SHO level. The energy level (known as the Landau level) is then

$$E_n = \hbar \omega_c \left( n + \frac{1}{2} \right) + \frac{\hbar^2 k_z^2}{2m}. \quad (2.5)$$

Although the energy level is discrete when the z-direction is restricted, as in two-dimensional materials, it contains macroscopic degeneracy at each level, which provides a non-trivial playground for the correlated system, such as the fractional quantum Hall effect. Assuming the system is restricted to the xy-plane with  $0 \leq x < L_x$  and  $0 \leq y < L_y$ . Under Landau gauge,  $k_y = 2\pi j/L_y$  label the degenerated states within each Landau level, where  $j$  is an integer due to the boundary condition of the y-direction. Moreover, the guiding center position  $x_c$  is restricted to  $0 \leq x_c(k_y) < L_x$ , resulting in  $0 \leq j < eBL_xL_y/h$ . Therfore, the Laudau level degeneracy (per spin) is

$$D = \Phi/\Phi_0, \quad (2.6)$$

where  $\Phi = BL_xL_y$  is the total flux through the system, and  $\Phi_0 = h/e$  is the flux quantum.

## 2.2 Generalized Bloch Conditions

After introducing the Landau level in a uniform magnetic field, we will consider in this section the electronic structure in the periodic potential and how the magnetic field affects the symmetry of the system.

Before we begin, we recall Bloch's theorem for periodic potentials. Consider an electron moves in a potential  $V(\mathbf{r})$  that is periodic on the Bravais lattice defined by vectors

$$\mathbf{R}_j = j_1 \mathbf{a}_1 + j_2 \mathbf{a}_2 + j_3 \mathbf{a}_3.$$

We define the translation operator  $\mathcal{T}(\mathbf{R}_j) = \exp\left[\frac{i}{\hbar}\mathbf{p} \cdot \mathbf{R}_j\right]$  such that  $\mathcal{T}(\mathbf{R}_j)\psi(\mathbf{r}) = \psi(\mathbf{r} + \mathbf{R}_j)$ . Then  $\{\mathcal{T}(\mathbf{R}_j)\}$  form an Abelian integer additive group with  $\mathcal{T}(\mathbf{R}_j)\mathcal{T}(\mathbf{R}'_j) = \mathcal{T}(\mathbf{R}_j + \mathbf{R}'_j)$ . It is evident that the Hamiltonian  $H = \frac{p^2}{2m} + V(\mathbf{r})$  is invariant under periodic translation, i.e.,  $\mathcal{T}(\mathbf{R}_j)H\mathcal{T}^{-1}(\mathbf{R}_j) = H$ . Consequently,  $[H, \mathcal{T}(\mathbf{R}_j)] = 0$ , indicating that  $H$  and  $\mathcal{T}(\mathbf{R}_j)$  share common eigen wave functions, named as the Bloch wave functions. The Bloch wave function can be expressed as

$$\psi_{\mathbf{k}}(\mathbf{r}) = e^{i\mathbf{k} \cdot \mathbf{r}} u_{\mathbf{k}}(\mathbf{r}), \quad (2.7)$$

where  $u_{\mathbf{k}}(\mathbf{r})$  is a periodic function on the Bravais lattice  $\{\mathbf{R}_j\}$  and  $\mathbf{k}$  is the crystal wave vector. It is easy to verify that  $\mathcal{T}(\mathbf{R}_j)\psi_{\mathbf{k}}(\mathbf{r}) = e^{i\mathbf{k} \cdot \mathbf{R}_j} \psi_{\mathbf{k}}(\mathbf{r})$ , hence  $e^{i\mathbf{k} \cdot \mathbf{R}_j}$  is a eigenvalue of  $\mathcal{T}(\mathbf{R}_j)$  and is also its one-dimensional linear representation.

We now introduce a uniform magnetic field into the periodic system. For three-dimensional systems, we require the magnetic field parallel to  $\mathbf{a}_3$ . For two-dimensional systems, we re-

quire the magnetic field perpendicular to the plane. The Hamiltonian is given by

$$H = \frac{1}{2m} \left( \mathbf{p} + e\mathbf{A}(\mathbf{r}) \right)^2 + V(\mathbf{r}). \quad (2.8)$$

Despite the uniformity of the magnetic field, the corresponding gauge vector potential breaks the translational symmetry. This can be illustrated by a simple argument. Let us assume that the system is restricted to two dimensions and the magnetic field is perpendicular to the plane. Consider an electron looping along the boundary of the unit cell. Upon returning to the origin, the electron acquires an Aharonov-Bohm phase equal to  $2\pi\Phi/\Phi_0$ , where  $\Phi$  is the magnetic flux of the unit cell. If the ratio  $\Phi/\Phi_0$  is not an integer, the phase of the electron differs from the initial phase. Consequently, the wave function of the electron cannot retain the identical periodic structure as the potential. However, if we assume that  $\Phi/\Phi_0 = p/q$  is a rational number, where  $p$  and  $q$  are integers, then we can expand the unit cell to a supercell  $q$  times larger. This implies that the flux through this supercell is  $p\Phi_0$ , and thus the corresponding Aharonov-Bohm phase is an integer multiple of  $2\pi$ . Consequently, the electronic wave function can be arranged in a periodic structure that is identical to that of the  $q$ -fold expanded sublattice.

In the following, we generalize Bloch's theorem to systems with uniform magnetic fields [17]–[19]. Consider a general vector potential  $\mathbf{A}(\mathbf{r}) = \mathcal{J}\mathbf{r}$  where  $\mathcal{J}$  is a linear map. We define the mechanical momentum operator  $\mathbf{\Pi} = \mathbf{p} + e\mathbf{A}(\mathbf{r})$  and conjugate momentum operator  $\bar{\mathbf{\Pi}} = \mathbf{p} + e\bar{\mathbf{A}}(\mathbf{r})$ , where  $\bar{\mathbf{A}}(\mathbf{r}) = \mathcal{J}^T\mathbf{r}$  is the conjugate vector potential satisfying  $\bar{\mathbf{A}}(\mathbf{r}_1) \cdot \mathbf{r}_2 = \mathbf{A}(\mathbf{r}_2) \cdot \mathbf{r}_1$ . It is easy to show that  $[\mathbf{\Pi}_i, \bar{\mathbf{\Pi}}_j] = 0$  and  $[x_i, \bar{\mathbf{\Pi}}_j] = i\hbar$ . Therefore,  $\bar{\mathbf{\Pi}}$  acts as a translation generator with the presence of the magnetic field. Now we define the magnetic translation operator

$$\mathcal{T}_m(\mathbf{R}_j) = e^{-i\pi j_1 j_2 \Phi/\Phi_0} \exp \left[ \frac{i}{\hbar} \bar{\mathbf{\Pi}} \cdot \mathbf{R}_j \right] \quad (2.9)$$

with  $\mathbf{R}_j = j_1 \mathbf{a}_1 + j_2 \mathbf{a}_2 + j_3 \mathbf{a}_3$ . One finds that  $H$  is invariant under magnetic translation,

$\mathcal{T}_m(\mathbf{R}_j)H\mathcal{T}_m^{-1}(\mathbf{R}_j) = \frac{1}{2m}\mathbf{\Pi}^2 + V(\mathbf{r} + \mathbf{R}_j) = H$ . Therefore,  $H$  and  $\mathcal{T}_m(\mathbf{R}_j)$  share common eigen wave functions. However, notice that if we loop around a parallelogram spanned by  $\mathbf{R}_j$  and  $\mathbf{R}'_j$ , a net phase is acquired as

$$\mathcal{T}_m^{-1}(\mathbf{R}'_j)\mathcal{T}_m^{-1}(\mathbf{R}_j)\mathcal{T}_m(\mathbf{R}'_j)\mathcal{T}_m(\mathbf{R}_j) = e^{2\pi i \mathbf{B} \cdot (\mathbf{R}_j \times \mathbf{R}'_j)/\Phi_0}. \quad (2.10)$$

Thus only if such phase is an integer multiple of  $2\pi$ , the magnetic translation  $\{\mathcal{T}_m(\mathbf{R}_j)\}$  form an Abelian group. As mentioned earlier, assuming rational number flux per unit cell  $\Psi/\Psi_0 = p/q$  and choose a enlarged sublattice such as

$$\mathbf{S}_j = j_1 \mathbf{a}_1 + j_2 (q \mathbf{a}_2) + j_3 \mathbf{a}_3, \quad j_1, j_2, j_3 \in \mathbb{Z}, \quad (2.11)$$

then operator  $\mathcal{T}_m(\mathbf{S}_j)$  fulfill Abelian additive relation  $\mathcal{T}_m(\mathbf{S}_j)\mathcal{T}_m(\mathbf{S}'_j) = \mathcal{T}_m(\mathbf{S}_j + \mathbf{S}'_j)$ . And the eigen wave function of  $\mathcal{T}_m(\mathbf{S}_j)$  is our desired generalized magnetic Bloch wave functions,

$$\mathcal{T}_m(\mathbf{S}_j)\psi_{\mathbf{k}}(\mathbf{r}) = e^{i\mathbf{k} \cdot \mathbf{S}_j} \psi_{\mathbf{k}}(\mathbf{r}), \quad (2.12)$$

where the magnetic crystal momentum  $\mathbf{k}$  can be restricted to the first Brillouin zone of  $\{\mathbf{S}_j\}$ . Rewriting  $\psi_{\mathbf{k}}(\mathbf{r}) = e^{i\mathbf{k} \cdot \mathbf{r}} u_{\mathbf{k}}(\mathbf{r})$ , we have the following magnetic Bloch condition on  $u_{\mathbf{k}}(x)$ ,

$$u_{\mathbf{k}}(\mathbf{r} + \mathbf{S}_j) = \exp\left[-\frac{i}{\hbar}e\mathbf{A}(\mathbf{S}_j) \cdot \mathbf{r}\right] u_{\mathbf{k}}(\mathbf{r}). \quad (2.13)$$

We will also refer to  $u_{\mathbf{k}}(\mathbf{r})$  as the magnetic Bloch wave function in the absence of ambiguity.

Next, we discuss the magnetic Bloch wave function in detail. We observe that  $e^{-\frac{i}{\hbar}e\mathbf{A}(\mathbf{S}_j) \cdot \mathbf{r}}$  in Eq. (2.13) is the momentum translation operator. Hence a shift of  $\mathbf{S}_j$  in real space for magnetic Bloch wave function is equivalent to a shift of  $\Delta\mathbf{k} = e\mathbf{A}(\mathbf{S}_j)/\hbar$  in reciprocal space. Take the Landau level wave function Eq. (2.4) for instance, where  $V(\mathbf{r}) = 0$  can be viewed as periodic potential. While the magnetic Bloch wave function  $\phi_n(x - x_c(k_y))$  is invariant in

y- and z-directions, the shift in x-direction resulting in a shift of the guiding center position  $x_c(k_y) - \Delta x = x_c(k_y + \Delta k_y)$ , which is equivalent to a shift in the  $k_y$ -direction. For a more general periodic potential, we define the reciprocal lattice

$$\mathbf{G} = n_1 \mathbf{b}_1 + n_2 \mathbf{b}_2 + n_3 \mathbf{b}_3, \text{ with } n_1, n_2, n_3 \in \mathbb{Z} \text{ and } \mathbf{a}_i \cdot \mathbf{b}_j = 2\pi\delta_{ij}. \quad (2.14)$$

Similar to the Landau level, we want to choose a gauge such that the magnetic Bloch wave function is periodic in the  $\mathbf{a}_2$ - and  $\mathbf{a}_3$ - directions, and a translation in the  $\mathbf{a}_1$ -direction contributes to a momentum shift in the  $\mathbf{b}_2$ -direction. This requires a modified Landau gauge

$$\mathbf{A} = \frac{p\hbar}{2\pi q} \mathbf{b}_2 \mathbf{b}_1 \cdot \mathbf{r}. \quad (2.15)$$

With the choice of such a gauge, the magnetic Bloch condition is simplified to

$$u_{\mathbf{k}}(\mathbf{r} + \mathbf{a}_1) = e^{-i\frac{p}{q}\mathbf{b}_2 \cdot \mathbf{r}} u(\mathbf{r}), \quad (2.16)$$

$$u_{\mathbf{k}}(\mathbf{r} + q\mathbf{a}_2) = u(\mathbf{r}), \quad (2.17)$$

$$u_{\mathbf{k}}(\mathbf{r} + \mathbf{a}_3) = u(\mathbf{r}). \quad (2.18)$$

## 2.3 Fractional Coordinates

For simplicity in subsequent derivations and calculations, we will use the following coordinate notation convention. For a function  $f(\mathbf{r})$  in the real space, we use the fractional coordinate

$$f(x_1, x_2, x_3) = f(x_1 \mathbf{a}_1 + x_2 \mathbf{a}_2 + x_3 \mathbf{a}_3) \quad (2.19)$$

The gradient operator can be expressed as

$$\nabla = \frac{1}{2\pi}(\mathbf{b}_1 \mathbf{a}_1 \cdot \nabla + \mathbf{b}_2 \mathbf{a}_2 \cdot \nabla + \mathbf{b}_3 \mathbf{a}_3 \cdot \nabla) \quad (2.20)$$

$$= \frac{1}{2\pi}(\mathbf{b}_1 \partial_{x_1} + \mathbf{b}_2 \partial_{x_2} + \mathbf{b}_3 \partial_{x_3}) \quad (2.21)$$

where  $\partial_{x_i} = \frac{\partial}{\partial x_i}$  is the partial derivative with respect to  $x_i$ . With the fractional coordinates, the mechanical momentum operator is simplified to

$$\Pi = \hbar \mathbf{b}_1 \tilde{\Pi}_1 + \hbar \mathbf{b}_2 \tilde{\Pi}_2 + \hbar \mathbf{b}_3 \tilde{\Pi}_3, \quad (2.22)$$

with dimensionless operators

$$\tilde{\Pi}_1 = -\frac{i}{2\pi} \partial_{x_1}, \quad \tilde{\Pi}_2 = -\frac{i}{2\pi} \partial_{x_2} + \frac{p}{q} x_1, \quad \tilde{\Pi}_3 = -\frac{i}{2\pi} \partial_{x_3}. \quad (2.23)$$

## 2.4 Numerical Methods

In this section, we discuss numerical methods for calculating the electronic structure in periodic potentials and uniform magnetic fields. The computational approaches can be broadly categorized into two groups: lattice methods, which are based on Wannier states or the tight-binding model, and real-space continuum methods. Both *ab initio* calculations and low-energy effective models of Moiré systems favor the continuum model. Consequently, our focus is primarily on the algorithmic implementation of the continuum model.

### 2.4.1 Plane-wave-based algorithms

Plane-wave-based methods are highly efficient for handling real-space continuum models, particularly in electronic structure calculations. These methods are especially advantageous because they simplify the computational challenges associated with the large dimensionality of the Hilbert space, which scales proportionally with the number  $N$  of grid points in

the model. The computational complexity of performing dense matrix-vector multiplications typically scales with the square of the Hilbert space dimension, making such operations challenging for large systems. However, the application of the Fast Fourier Transform (FFT) significantly accelerates these computations, making plane-wave methods a preferred approach.

The Hamiltonian in continuum models is typically divided into components: those involving derivatives (such as kinetic energy terms in the absence of a magnetic field) and those involving only coordinate functions (such as potential energy terms). The kinetic energy terms, which involve derivatives, are diagonal in the plane-wave basis, while the potential energy terms are diagonal in the real-space basis. This separation allows the computational complexity of applying each part of the Hamiltonian to the wavefunction to be  $\mathcal{O}(N)$ . The FFT facilitates efficient switching between the plane-wave and real-space representations, with a computational complexity of  $\mathcal{O}(N \ln N)$ . As a result, the overall complexity of applying the Hamiltonian to the wavefunction scales as  $\mathcal{O}(N \ln N)$ .

In traditional plane-wave algorithms without a magnetic field, the Bloch wavefunction  $u_{n\mathbf{k}}(x_1, x_2, x_3)$  (in the fractional coordinate Eq. (2.19)) is represented in reciprocal space by its Fourier components  $u_{n\mathbf{k}}(G_1, G_2, G_3)$ ,

$$u_{n\mathbf{k}}(x_1, x_2, x_3) = \sum_{G_1, G_2, G_3} u_{n\mathbf{k}}(G_1, G_2, G_3) e^{-i(G_1 x_1 + G_2 x_2 + G_3 x_3)} \quad (2.24)$$

where  $(G_1, G_2, G_3) \in (2\pi\mathbb{Z})^3$  is the reciprocal lattice vector. The transformation between real space and reciprocal space is typically performed using a multi-dimensional FFT.

However, when a magnetic field is introduced and the generalized Bloch conditions Eq. (2.16) are applied, the transformation process is modified [20], [21]. The wavefunction can no longer be transformed directly between real space and reciprocal space as usual. Instead, an intermediate space is introduced to facilitate the transformation. For the sake of simplicity, we consider the two-dimensional case involving only the  $x_1$ - and  $x_2$ -axis, since

$x_3$  is always periodic under the chosen gauge Eq. (2.15).

The wavefunction  $u_{n\mathbf{k}}(x_1, x_2)$  is first Fourier transformed along the  $x_2$ -axis to yield an intermediate function  $u_{n\mathbf{k}}(x_1, G_2/q)$ , where  $G_2/q \in 2\pi\mathbb{Z}$  is a reciprocal space variable corresponding to the enlarged superlattice, while  $x_1$  remains a real space variable. In this intermediate space, the generalized Bloch conditions impose a new relationship between the wavefunction components,

$$u(x_1 + 1, G_2/q) = u(x_1, G_2/q + 2\pi p/q). \quad (2.25)$$

This condition indicates that the wavefunction  $u(x_1, G_2/q)$  in intermediate space behaves like a spiral rather than a set of independent rings, as would be the case without a magnetic field. An introduction of a new variable  $\hat{x}_1 = x_1 + G_2/(2\pi p)$  effectively unwinds this spiral into a one-dimensional function. The transformed wavefunction  $u(\hat{x}_1) = u(x_1, G_2/q)$  is then subjected to a Fourier transform along the  $\hat{x}_1$ -axis, yielding a new set of Fourier coefficients  $u(\hat{G}_1/N_{\hat{x}_1})$ , where  $\hat{G}_1/N_{\hat{x}_1} \in 2\pi\mathbb{Z}$  and  $N_{\hat{x}_1}$  depends on the length truncation of  $\hat{x}_1$ -axis. These Fourier coefficients represent the wavefunction in a plane-wave-like, orthonormal basis that adheres to the generalized Bloch conditions. This two-step transformation process—first into an intermediate space and then into a reciprocal space—ensures that the plane-wave representation of the wavefunction properly accounts for the phase shifts introduced by the magnetic gauge field.

In the absence of a magnetic field, the Hamiltonian  $H$  in plane-wave-based calculations is typically decomposed into kinetic energy  $T$  and potential energy  $V$  components, which are diagonal in reciprocal and real space, respectively. The total Hamiltonian acting on a wavefunction,  $H |\psi\rangle$ , is then assembled using FFT.

When a magnetic field is present, and generalized Bloch conditions are applied, the Hamiltonian  $H$  can be decomposed into three components, each diagonal in a different

space,

$$H = \frac{\hbar^2}{2m} \left( \mathbf{b}_1 \tilde{\Pi}_1 + \mathbf{b}_2 \tilde{\Pi}_2 \right)^2 + V, \quad (2.26)$$

where  $\tilde{\Pi}_1 = \frac{\hat{G}_1}{2\pi}$  is diagonal in reciprocal space representation  $u(\hat{G}_1)$ ;  $\tilde{\Pi}_2 = \frac{G_2}{2\pi q} + \frac{p}{q}x_1$  is diagonal in the intermediate space representation  $u(x_1, G_2/q)$ ;  $V$  (the potential energy) remains diagonal in real space. These components are computed separately in their respective spaces, and the total action of Hamiltonian on a wavefunction  $H|\psi\rangle$  is assembled via FFT, similar to the zero-field case. This approach allows for efficient handling of the complexities introduced by the magnetic field, ensuring that the computational cost remains manageable even for large systems.

#### 2.4.2 Conjugate gradient method

The Conjugate Gradient (CG) method is a powerful iterative technique widely used for solving large linear systems [22], [23], particularly those encountered in plane-wave-based approaches in quantum mechanics. This method is especially effective for systems where the matrix is symmetric and positive definite, making it ideal for ab initio calculations and eigenproblems encountered in electronic structure calculations.

In plane-wave-based electronic structure calculations, the CG method is frequently employed to iteratively optimize electronic wavefunctions. Its efficiency is particularly beneficial in density functional theory (DFT) calculations, where it allows for rapid convergence of wavefunctions following updates to the self-consistent field (SCF), typically requiring only a few iterations. Each electronic state (or band) is treated independently through band-by-band CG optimization.

The CG method is applied to minimize a quadratic form associated with the Schrödinger

equation,

$$H |\psi_{n\mathbf{k}}\rangle = \lambda |\psi_{n\mathbf{k}}\rangle, \quad (2.27)$$

where  $H$  is the Hamiltonian matrix,  $|\psi_{n\mathbf{k}}\rangle$  is the (magnetic) Bloch wave-function with momentum  $\mathbf{k}$  and band index  $n$ , and  $\lambda$  is the corresponding eigen-energy. This eigenproblem can be represented by the local minimum problem of a quadratic form

$$\mathcal{L} = \frac{1}{2} \langle \psi_{n\mathbf{k}} | H | \psi_{n\mathbf{k}} \rangle - \frac{1}{2} \lambda (\langle \psi_{n\mathbf{k}} | \psi_{n\mathbf{k}} \rangle - 1), \quad (2.28)$$

where  $\lambda$  is recognized as the Lagrange multiplier for wave-function normalization. The CG method iteratively updates the wave-function  $|\psi_{n\mathbf{k}}\rangle$  to minimize  $\mathcal{L}$ , effectively solving the eigenvalue problem.

The convergence rate of the CG method is influenced by the condition number  $\kappa_H$  of the Hamiltonian matrix  $H$ . The CG method's complexity scales as  $\mathcal{O}(\sqrt{\kappa_H})$ , offering a significant improvement over the steepest descent method, which scales as  $\mathcal{O}(\kappa_H)$ . For well-conditioned systems, this leads to a much faster solution. In comparison, the steepest descent method is a simpler approach for minimizing a quadratic form, but it is less efficient due to its tendency to follow the gradient direction in a zigzag manner, which slows down convergence. The CG method, on the other hand, constructs a series of mutually conjugate directions, which reduces the zigzagging and accelerates convergence.

The detailed CG algorithm is as follows. For given momentum  $\mathbf{k}$ , the algorithm begins with an initial guess for the wave-functions  $|\psi_{n\mathbf{k}}^{(0)}\rangle$  of the lowest  $N_b$  bands, ensuring they are orthogonally normalized. The following iterative process is then employed: At  $i$ -th iteration, we optimize each wave-function  $|\psi_{n\mathbf{k}}^{(i)}\rangle$  by first calculating the conjugate gradient direction and then doing the line search with respect to the conjugate gradient direction. We define

the gradient vector as

$$\left| g_n^{(i)} \right\rangle = \left( 1 - \sum_{n'=1}^{N_b} \left| \psi_{n'k}^{(i)} \right\rangle \left\langle \psi_{n'k}^{(i)} \right| \right) (\lambda_n^{(i)} - H) \left| \psi_{nk}^{(i)} \right\rangle \quad (2.29)$$

with  $\lambda_n^{(i)} = \left\langle \psi_{nk}^{(i)} \right| H \left| \psi_{nk}^{(i)} \right\rangle$ . Here, we have made  $\left| g_n^{(i)} \right\rangle$  orthogonal to all  $\left| \psi_{nk}^{(i)} \right\rangle$ -s. The conjugate gradient direction is calculated by

$$\left| d_n^{(i)} \right\rangle = \left| g_n^{(i)} \right\rangle + \beta_n^{(i)} \left| d_n^{(i-1)} \right\rangle, \quad (2.30)$$

where  $\beta_n^{(i)} = \left\langle g_n^{(i)} \right| g_n^{(i)} \rangle / \left\langle g_n^{(i-1)} \right| g_n^{(i-1)} \rangle$  and  $\beta_n^{(0)} = 0$ . For the line search, we deal with the single-parameter minimization of

$$E(\theta) = \left\langle \psi_{nk}^{(i+1)} \right| H \left| \psi_{nk}^{(i+1)} \right\rangle \quad (2.31)$$

with

$$\left| \psi_{nk}^{(i+1)} \right\rangle = \cos \theta \left| \psi_{nk}^{(i)} \right\rangle + \sin \theta \left| d_n^{(i)} \right\rangle. \quad (2.32)$$

A good approximation of  $E(\theta)$  is

$$E(\theta) = E_0 + E_c \cos \theta (2\theta) + E_s \sin (2\theta), \quad (2.33)$$

according to which it is easy to find the minimal solution  $\left| \psi_{nk}^{(i+1)} \right\rangle$ . Here,  $E_0$ ,  $E_c$  and  $E_s$  are determined by evaluating  $E(\theta = 0)$ ,  $E(\theta = \pi/300)$ , and

$$\frac{\partial E(\theta)}{\partial \theta} \Big|_{\theta=0} = 2 \operatorname{Re} \left\{ \left\langle d_n^{(i)} \right| H \left| \psi_{nk}^{(i)} \right\rangle \right\}. \quad (2.34)$$

To further accelerate the CG method, preconditioning techniques are often used, by

modifying the gradient vector Eq. (2.29) by

$$\left| g_n^{(i)} \right\rangle = \left( 1 - \sum_{n'=1}^{N_b} \left| \psi_{n'k}^{(i)} \right\rangle \left\langle \psi_{n'k}^{(i)} \right| \right) K_n^{(i)} (\lambda_n^{(i)} - H) \left| \psi_{nk}^{(i)} \right\rangle \quad (2.35)$$

where  $K_n^{(i)}$  is the preconditioning matrix. Preconditioning improves the condition number of the Hamiltonian, leading to faster convergence. A practical choice of the preconditioning matrix is

$$K_n^{(i)} = \sum_{\mathbf{G}} |\mathbf{G}\rangle \frac{27 + 18x + 12x^2 + 8x^3}{27 + 18x + 12x^2 + 8x^3 + 16x^4} \langle \mathbf{G}|, \quad (2.36)$$

where  $\langle \mathbf{r} | \mathbf{G} \rangle = e^{i\mathbf{G} \cdot \mathbf{r}}$  is the plane-wave with the reciprocal vector  $\mathbf{G}$  as its momentum, and  $x = \frac{\hbar^2 G^2}{2m_e} / \lambda_n^{(i)}$ .

In summary, the CG method, when used in conjunction with plane-wave-based approaches, is a highly efficient tool for solving the Schrödinger equation in periodic potentials and uniform magnetic fields. Its ability to solve eigenproblems rapidly, combined with preconditioning and other optimization techniques, makes it an essential method in modern electronic structure calculations.

However, it is important to note that the convergence rate of the CG method can be significantly affected by the energy gap above the highest calculated band. If this energy gap is small, the method converges more slowly. This issue is particularly severe when calculating the Hofstadter spectrum, especially for systems with magnetic flux  $\Psi = \frac{p}{q}\Psi_0$  where  $q$  is large. In such cases, the number of bands is proportional to  $q$ , and the small energy gaps between them make convergence challenging. The densely packed bands require careful handling to achieve accurate and efficient convergence, often necessitating additional computational resources.

### 2.4.3 Relaxation Method

The relaxation method is a numerical technique employed to solve the time-independent Schrödinger equation, particularly useful for determining the ground state and low-lying excited states of quantum systems, and is complementary to the CG method for Hofstadter problem with large  $q$  [24]–[26]. The method is based on the evolution of the wavefunction in imaginary time, allowing it to converge towards the eigenstates of the Hamiltonian. The use of high-order Trotter decomposition in this method significantly improves both the accuracy and efficiency of the computation.

Imaginary time propagation transforms the time evolution of a quantum state into a process that naturally filters out higher-energy states. Starting with an initial guess for  $N_{\text{basis}}$  low-energy eigenfunctions  $\{|\psi_j\rangle\}_{j=1}^{N_{\text{basis}}}$ , the wavefunctions is evolved according to

$$|\psi_j; \tau\rangle = e^{-\tau H/\hbar} |\psi_j\rangle \quad (2.37)$$

where  $\tau$  is the imaginary time. As  $\tau$  increases, the wavefunction set  $\{|\psi_j; \tau\rangle\}$  converges towards the ground-state, because the higher-energy components decay exponentially faster. Periodically inserting orthogonalization of  $\{|\psi_j; \tau\rangle\}$  to the imaginary time evolution, e.g., using the column pivoting QR decomposition, ensures that the wavefunction set converges to the low-energy subspace without loss of dimension.

The evolution operator  $e^{-\tau H/\hbar}$  is generally difficult to compute directly. Instead, we approximate it using the Trotter decomposition, which splits the Hamiltonian into kinetic and potential energy parts  $H = T + V$  where  $T$  is the kinetic energy operator and  $V$  is the potential energy operator. The second-order Trotter decomposition for a small  $\tau$  is

$$\mathcal{T}_2(\tau) = e^{-\tau V/2\hbar} e^{-\tau T/\hbar} e^{-\tau V/2\hbar}. \quad (2.38)$$

While this decomposition is effective, it requires small time steps for accurate results. To

achieve higher accuracy with larger time steps, we use a higher-order Trotter decomposition [25]

$$e^{-\tau H} = \sum_{k=1}^n c_k \mathcal{T}_2^k(\tau/k) + \mathcal{O}(\tau^{2n+1}), \quad (2.39)$$

where  $c_k = \prod_{l=1(\neq k)}^n \frac{l^2}{l^2 - k^2}$  and  $\mathcal{T}_2$  is the second-order Trotter decomposition. For instance, the 6th-order ( $n = 3$ ) decomposition can be written as

$$e^{-\tau H/\hbar} \simeq \frac{1}{24} \mathcal{T}_2(\tau) - \frac{16}{15} \mathcal{T}_2^2(\tau/2) + \frac{81}{40} \mathcal{T}_2^3(\tau/3). \quad (2.40)$$

This method cancels out lower-order errors, allowing for more accurate approximations over larger time steps.

The high-order Trotter decomposition offers several significant advantages over lower-order methods. It enhances accuracy by eliminating lower-order errors, allowing for the use of larger time steps without compromising precision. This, in turn, leads to faster convergence, as the need for fewer iterations speeds up the overall computation. Additionally, the method is highly efficient in its implementation, particularly in the application of kinetic energy through FFT operations, making it well-suited for large-scale simulations on high-performance computing systems.

When applying high-order Trotter decomposition to quantum systems in the presence of a homogeneous magnetic field, special considerations are necessary due to the altered nature of the kinetic energy operator. Unlike system without magnetic field, where the kinetic energy  $T$  is diagonalized in the plane-wave basis, the presence of a magnetic field modifies the kinetic energy operator as

$$T = \frac{\hbar^2}{2m} \left( \mathbf{b}_1 \tilde{\Pi}_1 + \mathbf{b}_2 \tilde{\Pi}_2 \right)^2 \quad (2.41)$$

where  $[\tilde{\Pi}_2, \tilde{\Pi}_1] = \frac{p_i}{2\pi q} \neq 0$ . This non-commutativity prevents  $T$  from being simply diagonal-

ized in the usual plane-wave basis.

To illustrate the decomposition scheme for  $e^{-\tau T/\hbar}$ , we first consider an orthorhombic lattice where the kinetic energy can be expressed as

$$T = \frac{\hbar^2 \mathbf{b}_1^2}{2m} \tilde{\Pi}_1^2 + \frac{\hbar^2 \mathbf{b}_2^2}{2m} \tilde{\Pi}_2^2. \quad (2.42)$$

In order to find a decomposition scheme of  $e^{-\tau T}$ , we draw an analogy with the one-dimensional simple harmonic oscillator (SHO) with Hamiltonian

$$H_{\text{SHO}} = \frac{1}{2m} P^2 + \frac{1}{2} m \omega^2 Q^2 \quad (2.43)$$

where  $[Q, P] = i\hbar$ . The propagator for the SHO is well-known and given by

$$\langle q_1 | e^{-\frac{\tau}{\hbar} H_{\text{SHO}}} | q_2 \rangle = \sqrt{\frac{m\omega}{2\pi\hbar \sinh(\omega\tau)}} e^{-\frac{m\omega}{2\hbar \sinh(\omega\tau)} ((q_1^2 + q_2^2)(\cosh(\omega\tau) - 1) + (q_1 - q_2)^2)}. \quad (2.44)$$

It follows that the evolution operator for the SHO can be factorized as

$$e^{-\tau H_{\text{SHO}}/\hbar} = e^{-c_1(\tau) \frac{1}{2} m \omega^2 Q^2} e^{-c_2(\tau) \frac{1}{2m} P^2} e^{-c_1(\tau) \frac{1}{2} m \omega^2 Q^2}, \quad (2.45)$$

where the coefficients are

$$c_1(\tau) = \frac{\cosh(\omega\tau) - 1}{\hbar\omega \sinh(\omega\tau)}, \quad c_2(\tau) = \frac{\sinh(\omega\tau)}{\hbar\omega}. \quad (2.46)$$

By identifying  $P = \hbar b_1 \tilde{\Pi}_1$ ,  $Q = \frac{2\pi q}{pb_1} \tilde{\Pi}_2$ , and  $\omega = \frac{eB}{m}$ , we recover the commutation relation  $[Q, P] = i\hbar$ , and recognize that  $T$  is analogous to  $H_{\text{SHO}}$ . This analogy leads to the decomposition

$$e^{-\tau T/\hbar} = e^{-c_1(\tau) \frac{\hbar^2 \mathbf{b}_2^2}{2m} \tilde{\Pi}_2^2} e^{-c_2(\tau) \frac{\hbar^2 \mathbf{b}_1^2}{2m} \tilde{\Pi}_1^2} e^{-c_1(\tau) \frac{\hbar^2 \mathbf{b}_2^2}{2m} \tilde{\Pi}_2^2}, \quad (2.47)$$

where the operators  $e^{-c_1(\tau)\frac{\hbar^2 b_2^2}{2m}\tilde{\Pi}_2^2}$  and  $e^{-c_2(\tau)\frac{\hbar^2 b_1^2}{2m}\tilde{\Pi}_1^2}$  can be diagonalized in the  $u(\hat{G}_1)$  and  $u(x_1, G_2/q)$  representations, respectively, as illustrated in section 2.4.1.

After discussing the orthorhombic lattice, we generalize Eq. (2.47) to an unspecified lattice, with the magnetic field parallel to  $\mathbf{a}_3$ . For simplicity, We focus on the two-dimensional case involving only the  $x_1$ - and  $x_2$ -axes. The kinetic energy then becomes

$$T = \frac{\hbar^2}{2m} \left( b_1^2 \tilde{\Pi}_1^2 + b_1 b_2 \cos \theta \{ \tilde{\Pi}_1, \tilde{\Pi}_2 \} + b_2^2 \tilde{\Pi}_2^2 \right), \quad (2.48)$$

where  $\theta$  is the angle between  $\mathbf{b}_1$  and  $\mathbf{b}_2$ . By analogy with the SHO squeeze operator, the following relation holds,

$$e^{-i\lambda\tilde{\Pi}_2^2/2} \tilde{\Pi}_1 e^{i\lambda\tilde{\Pi}_2^2/2} = \tilde{\Pi}_1 + \frac{p}{2\pi q} \lambda \tilde{\Pi}_2. \quad (2.49)$$

Setting  $\lambda = \frac{2\pi q}{p} \frac{b_2}{b_1} \cos \theta$ , we find

$$T = \frac{\hbar^2}{2m} e^{-i\lambda\tilde{\Pi}_2^2/2} \left( b_1^2 \tilde{\Pi}_1^2 + b_2^2 \tilde{\Pi}_2^2 \sin^2 \theta \right) e^{i\lambda\tilde{\Pi}_2^2/2}, \quad (2.50)$$

leading to the generalized decomposition scheme

$$e^{-\tau T/\hbar} = e^{-\left(c_1(\tau)\frac{(\hbar b_2 \sin \theta)^2}{2m} + i\frac{\lambda}{2}\right)\tilde{\Pi}_2^2} e^{-c_2(\tau)\frac{\hbar^2 b_1^2}{2m}\tilde{\Pi}_1^2} e^{-\left(c_1(\tau)\frac{(\hbar b_2 \sin \theta)^2}{2m} - i\frac{\lambda}{2}\right)\tilde{\Pi}_2^2}. \quad (2.51)$$

With the use of high-order Trotter decomposition and the derived kinetic exponential decomposition, the imaginary time evolution operator can be expressed as a series of exponentials, each containing either the kinetic energy operator  $T$  or the momentum operators  $\tilde{\Pi}_1$  and  $\tilde{\Pi}_2$ . This decomposition allows each exponential term to be diagonalized in the corresponding representations— $u(\hat{G}_1)$  for  $\tilde{\Pi}_1$ ,  $u(x_1, G_2/q)$  for  $\tilde{\Pi}_2$ , and  $u(x_1, x_2)$  for  $V$ . Additionally, each exponential is numerically stable, as the absolute values of their eigenvalues are all less than one (suppose  $V > 0$ ), ensuring that the method is not only efficient and

accurate but also robust for large-scale simulations of the system.

# Chapter 3

## Hofstadter Physics of Moiré Transition Metal Dichalcogenides

### 3.1 Introduction

The Hofstadter butterfly, first predicted by Douglas Hofstadter in 1976, is one of the most iconic phenomena in condensed matter physics. It describes a fractal energy spectrum that emerges when electrons in a two-dimensional lattice are subjected to a perpendicular magnetic field. The interplay between the magnetic flux and the periodic potential of the lattice gives rise to a complex pattern of energy levels, resembling a butterfly in its structure. Historically, the Hofstadter butterfly has provided profound insights into the nature of quantum Hall effects and the topological properties of electronic systems [11], [14].

The advent of Moiré materials has opened a new regime for the study of Bloch electrons under a magnetic field [27], [28]. Moiré superlattices, such as those found in twisted bilayer graphene and transition metal dichalcogenides (TMD), feature a superlattice period that is much larger than the atomic spacing, often comparable to the magnetic length at  $B = 1\text{T}$  (26 nm). Additionally, the superlattice potential that creates minibands in these materials is weak and slowly varying. As a result of both features, the interplay between Landau

quantization and the superlattice potential can give rise to a complex energy spectrum and novel quantum phenomena not found in ordinary solids [29]–[31].

In recent years, the study of Hofstadter physics has gained renewed attention due to the emergence of Moiré superlattices [8], [10]. When two layers of TMD are stacked with a small twist angle, a large-scale Moiré pattern forms, creating a new periodic potential that significantly alters the electronic properties of the system. This phenomenon is not unique to TMD; it is also observed in other Moiré materials, such as twisted bilayer graphene and van der Waals heterostructures. These materials share the characteristic of having an enlarged Moiré unit cell compared to their atomic lattice, which significantly enlarges the accessible magnetic flux per unit cell. Consequently, they provide an unprecedented platform for exploring Hofstadter physics at experimentally achievable magnetic field strengths. In these systems, the Moiré-induced superlattice interacts with the applied magnetic field to produce a rich and intricate Hofstadter spectrum, revealing new insights into the electronic structure and topological properties of these materials [32], [33].

The exact calculation of the Hofstadter butterfly spectrum has been extensively studied in Moiré superlattices, particularly in twisted bilayer graphene [27], [34]. However, similar detailed studies for Moiré TMD systems are still lacking, making it a fertile area for further exploration.

The significance of studying Hofstadter physics in TMD systems lies in the potential applications in quantum materials. The enlarged Moiré unit cell facilitates the observation of integer quantum Hall effects (IQHE) and fractional quantum Hall effects (FQHE) at much lower magnetic fields than in conventional systems [9], [35]. These effects are not only of fundamental interest but also hold promise for developing new quantum technologies, such as topologically protected quantum computing and high-precision metrology. Furthermore, the interplay between strong spin-orbit coupling, electron correlations, and the Hofstadter spectrum in TMD opens up possibilities for discovering new quantum phases and exploring the boundaries of topological physics [36].

In this chapter, we will delve into the Hofstadter physics of twisted bilayer TMD. We will introduce the continuum model that describes the electronic properties of these systems and use this model to calculate the Hofstadter spectrum. Through this exploration, we aim to uncover how the unique properties of TMD, such as their large-scale Moiré patterns and strong spin-orbit interactions, lead to novel manifestations of Hofstadter physics and its associated quantum phenomena.

## 3.2 Continuum Model of TMD

As outlined in the introduction, twisted bilayer TMD have emerged as a rich platform for exploring novel electronic and topological phenomena. Central to understanding these phenomena is the continuum model, which captures the essential low-energy physics of these systems. In this section, we derive the continuum model for Moiré TMD systems [37], with a specific focus on the effective Hamiltonian that governs the electronic properties near the  $K$  and  $K'$  points in the Brillouin zone.

When two layers of TMD are stacked with a small twist angle or slight lattice mismatch, a Moiré superlattice forms, giving rise to new electronic structures and phenomena. This Moiré superlattice introduces a periodic potential that significantly modifies the band structure of the system, particularly in the vicinity of the  $K$  and  $K'$  points, due to the strong spin-orbit coupling and the valley degree of freedom inherent in TMD.

Let us first consider the case of an aligned bilayer TMD system, where the two layers are perfectly stacked without any twist. Since  $K$  and  $K'$  valley are related by the time-reversal symmetry, we can focus on the  $K$  valley, with the  $K'$  part Hamiltonian being its time-reversal partner. Additionally, spin-valley locking, induced by the strong spin-orbit coupling, binds spin- $\uparrow$  ( $\downarrow$ ) states to the  $K$  ( $K'$ ) valley. The Hamiltonian for the  $K$  valley can be expressed

as a two-band  $kp$  model that accounts for the layer degree of freedom

$$H_{\uparrow}(\theta = 0, \mathbf{d}_0) = \begin{pmatrix} \frac{\mathbf{p}^2}{2m^*} + \Delta_b(\mathbf{d}_0) & \Delta_T(\mathbf{d}_0) \\ \Delta_T^\dagger(\mathbf{d}_0) & \frac{\mathbf{p}^2}{2m^*} + \Delta_t(\mathbf{d}_0) \end{pmatrix} \quad (3.1)$$

where  $\Delta_b$  and  $\Delta_t$  are the on-site energies in the bottom and top layers, respectively, and  $\Delta_T$  is the inter-layer tunneling amplitude. The in-plane displacement between the two layers is denoted by  $\mathbf{d}_0$ . The effective mass  $m^*$  characterizes the curvature of the band near the  $K$  point. Note that we have used a hole representation with  $m^* > 0$ , whereas some literature may use an electron representation with  $m^* < 0$ .

When the two TMD layers are twisted by a small angle  $\theta$ , the in-plane displacement between the layers becomes position-dependent and can be expressed as  $\mathbf{d}(\mathbf{r}) = \theta \hat{z} \times \mathbf{r}$ . The momentum space is also affected by the twist, leading to a momentum shift  $\boldsymbol{\kappa}_{\pm} = \pm(\theta/2)\hat{z} \times K$  in the Dirac points (+ for the top layer and - for the bottom layer). The effective Hamiltonian for the twisted bilayer is then modified as

$$H_{\uparrow}(\mathbf{r}) = \begin{pmatrix} \frac{(\mathbf{p} - \hbar\boldsymbol{\kappa}_+)^2}{2m^*} + \Delta_b(\mathbf{r}) & \Delta_T(\mathbf{r}) \\ \Delta_T^\dagger(\mathbf{r}) & \frac{(\mathbf{p} - \hbar\boldsymbol{\kappa}_-)^2}{2m^*} + \Delta_t(\mathbf{r}) \end{pmatrix}. \quad (3.2)$$

The terms  $\Delta_b(\mathbf{r})$ ,  $\Delta_t(\mathbf{r})$ , and  $\Delta_T(\mathbf{r})$  now vary with position  $\mathbf{r}$ , reflecting the Moiré pattern. This position dependence is a key feature of the continuum model, capturing the modulated electronic environment in the Moiré superlattice.

Given the periodic nature of the Moiré pattern, the spatially varying potentials  $\Delta_\alpha(\mathbf{r})$  (where  $\alpha = b, t, T$ ) are periodic in the Moiré superlattice, with Moiré reciprocal lattice vectors  $\{\mathbf{G}\}$ , and can be expanded as a Fourier series

$$\Delta_\alpha(\mathbf{r}) = \sum_{\mathbf{G}} \Delta_\alpha(\mathbf{G}) e^{i\mathbf{G} \cdot \mathbf{r}}, \quad (3.3)$$

where  $\Delta_\alpha(\mathbf{G})$  are the corresponding Fourier coefficients. In the lowest harmonic approxi-

mation, we simplify the Fourier expansion by retaining only the terms corresponding to the smallest reciprocal lattice vectors, i.e., the first shell reciprocal lattice vectors  $|\mathbf{G}| = G_0$ , where  $G_0$  is the magnitude of the smallest reciprocal lattice vector. These terms typically dominate the electronic structure near the  $K$  and  $K'$  points due to their long-wavelength nature. We label the the first shell reciprocal lattice vectors by counterclockwise rotation of  $\mathbf{G}_1 = (4\pi)/(\sqrt{3}a_0)\hat{x}$  by angle  $(j - 1)\pi/3$ , with  $a_0$  the lattice constant of the monolayer TMD. Thus, we approximate

$$\Delta_\alpha(\mathbf{r}) \approx \sum_{j=1}^6 \Delta_\alpha(\mathbf{G}_j) e^{i\mathbf{G}_j \cdot \mathbf{r}}. \quad (3.4)$$

This approximation captures the essential features of the Moiré potential, while neglecting higher-order harmonics that contribute less significantly to the low-energy physics.

The dependence of  $\Delta_\alpha$  on  $\mathbf{r}$  is determined by the symmetry properties of the bilayer system. A mirror reflection across the z-axis interchanges the bottom (b) and top (t) layers and maps the in-plane displacement  $\mathbf{d}(\mathbf{r}) = \theta\hat{z} \times \mathbf{r}$  to  $\mathbf{d}(\mathbf{r}) = -\theta\hat{z} \times \mathbf{r}$ , leading to the relation  $\Delta_t(\mathbf{r}) = \Delta_b(-\mathbf{r})$ . Additionally, threefold rotational symmetry around the z-axis requires that  $\Delta_t(\mathbf{r})$  and  $\Delta_b(\mathbf{r})$  remain unchanged when  $\mathbf{r}$  is rotated by  $2\pi/3$ . These symmetry constraints result in the following two-parameter lowest-harmonic parametrization,

$$\Delta_l(\mathbf{r}) = -2V \sum_{j=1,3,5} \cos(\mathbf{G}_j \cdot \mathbf{r} + l\psi) \quad (3.5)$$

where  $l = 1$  for the top layer and  $l = -1$  for the bottom layer.

For the inter-layer hopping  $\Delta_T(\mathbf{r})$ , we must first account for the momentum shift between the two layers by  $\boldsymbol{\kappa}_+$  and  $\boldsymbol{\kappa}_-$ , which introduces an intrinsic momentum difference  $\Delta\boldsymbol{\kappa} = \boldsymbol{\kappa}_- - \boldsymbol{\kappa}_+$  in the inter-layer hoping. Due to the threefold rotational symmetry, the smallest inter-layer momentum differences  $\Delta\mathbf{G}_{\text{down}} = \Delta\boldsymbol{\kappa}$ ,  $\Delta\mathbf{G}_{\text{upper right}} = \mathbf{G}_2 + \Delta\boldsymbol{\kappa}$ , and  $\Delta\mathbf{G}_{\text{upper left}} = \mathbf{G}_3 + \Delta\boldsymbol{\kappa}$ , share the same hopping amplitude. Consequently, the lowest-

harmonic parametrization of  $\Delta_T(\mathbf{r})$  is given by

$$\Delta_T(\mathbf{r}) = w(1 + e^{i\mathbf{G}_2 \cdot \mathbf{r}} + e^{i\mathbf{G}_3 \cdot \mathbf{r}}). \quad (3.6)$$

The pseudo-layer-spin texture of the Moiré potential described by

$$\Delta(\mathbf{r}) = \left( \text{Re}\{\Delta_T^\dagger\}, \text{Im}\{\Delta_T^\dagger\}, \frac{1}{2}(\Delta_t - \Delta_b) \right) \quad (3.7)$$

forms a skyrmion lattice in real space. A skyrmion is a topologically protected configuration where the pseudo-spin vector covers the entire unit sphere once over a Moiré unit cell. Quantitatively, the winding number

$$N_w = \frac{1}{4\pi} \int \frac{\Delta \cdot (\partial_x \Delta \times \partial_y \Delta)}{|\Delta|^3} d\mathbf{r}^2 = -1 \quad (3.8)$$

indicating a topologically non-trivial configuration. This skyrmion texture in real space is linked to the Berry curvature in momentum space, contributing to the non-zero Chern number of the Moiré bands.

Building on the continuum model derived earlier, we next delve into the band structure of twisted bilayer TMD systems. Specifically, we choose  $\phi = -91^\circ$ ,  $V = 11.2$  meV,  $w = -13.3$  meV, and  $m = 0.62 m_e$  for twisted MoTe<sub>2</sub> homobilayer system [38] with monolayer lattice constant  $a_0 = 3.52$  Å. The introduction of a twist angle  $\theta$  between the layers creates a Moiré superlattice, which effectively folds the electronic bands into a smaller Brillouin zone. This folding leads to the formation of Moiré bands, particularly affecting the electronic states near the  $K$  and  $K'$  valleys due to the long-wavelength periodic potential induced by the Moiré pattern. The Moiré band structures with different twist angles  $\theta$  are shown in Fig. 3.1.

As the twist angle  $\theta$  decreases, these Moiré bands become increasingly flat, resulting in a very narrow bandwidth. The flattening of the bands significantly enhances the density of states, which in turn amplifies electron-electron interactions. This phenomenon is crucial as

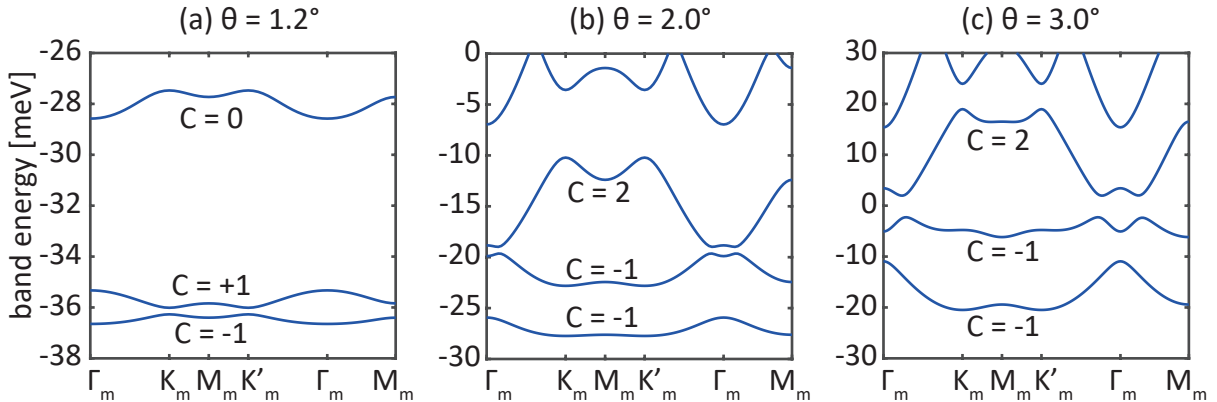


Figure 3.1: Moiré band structure of twisted MoTe<sub>2</sub> homobilayer with twist angle (a)  $\theta = 1.2^\circ$ , (b)  $\theta = 2.0^\circ$ , and (c)  $\theta = 3.0^\circ$ . The Chern numbers  $C$  of each band is labeled in valley  $K$ , while  $C$  should change sign in valley  $K'$  due to the time-reversal symmetry.

it can give rise to correlated electronic phases such as Mott insulators and superconductivity.

The Moiré superlattice not only modifies the band structure but also introduces non-trivial topological properties. In TMD bilayers, such as MoTe<sub>2</sub>, the interplay between the Moiré potential and strong spin-orbit coupling can lead to the emergence of topologically non-trivial bands. These bands are characterized by quantized topological invariants, such as the Chern number, which describes the winding of the Berry phase across the Brillouin zone. In Moiré TMD systems, the topmost Moiré valence bands near the  $K$  valley can exhibit non-trivial Chern numbers. The numerically calculated Berry curvatures of the low energy bands with different twist angles  $\theta$  are shown in Fig. 3.2. A non-zero Chern number indicates that these bands are topologically protected, which paves the way for the observation of quantum Hall-like effects without the need for an external magnetic field, a phenomenon known as the quantum anomalous Hall effect (QAHE). Moreover, a evenly distributed Berry curvatures at  $\theta = 2.0^\circ$  indicate a possible fractional Chern insulator (FCI) candidate if turn on the interaction.

Moreover, the Moiré bands in TMD can realize a Kane-Mele-type quantum spin Hall effect, where the system exhibits edge states that are protected by time-reversal symmetry. These edge states are a direct manifestation of the non-trivial topology of the bulk bands,

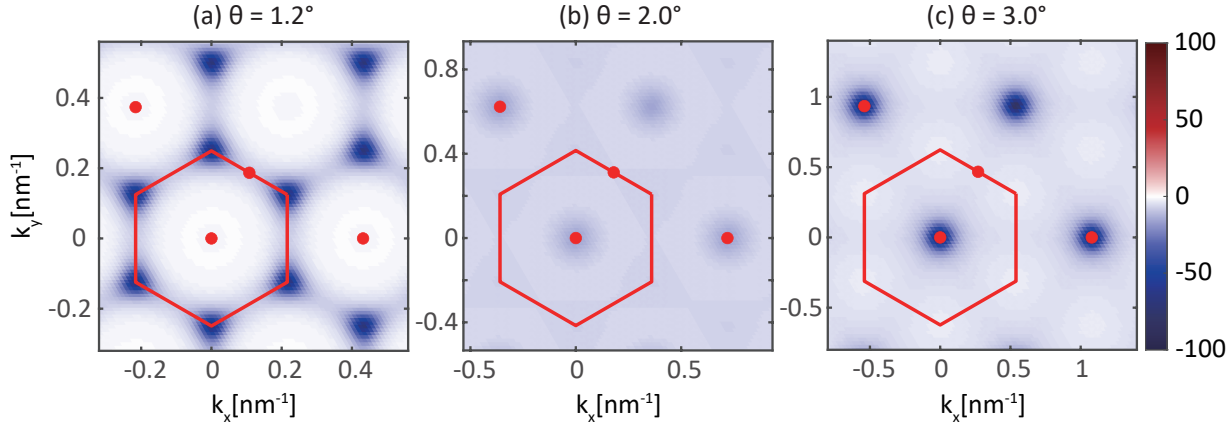


Figure 3.2: Berry curvatures of the lowest energy band for a  $\text{MoTe}_2$  homobilayer at the  $K$  valley, with twist angles: (a)  $\theta = 1.2^\circ$ , (b)  $\theta = 2.0^\circ$ , and (c)  $\theta = 3.0^\circ$ . The Berry curvature exhibits a sign change at the  $K'$  valley. The calculated Chern numbers for all three twist angles are  $C = -1$ , which would also reverse sign at the  $K'$  valley.

and they enable quantized conductance even in the absence of a magnetic field. The presence of such topologically protected edge states makes twisted bilayer TMD promising candidates for exploring new quantum phases and potentially developing novel quantum devices.

### 3.3 Hofstadter Spectrum in Moiré TMD

In this section, we explore the Hofstadter spectrum that emerges in Moiré TMD systems under an external magnetic field. Building on the continuum model developed earlier, we analyze the interplay between the Moiré superlattice and the magnetic field, which gives rise to the intricate fractal pattern known as the Hofstadter butterfly.

The effective Hamiltonian governing the low-energy physics near the  $K$  and  $K'$  points in Moiré TMD is the foundation for our analysis. When a perpendicular magnetic field is applied, the periodic potential of the Moiré superlattice interacts with the magnetic field, leading to the formation of Landau levels that are modulated by the Moiré potential. This interplay results in the fractal Hofstadter spectrum.

Under an external perpendicular magnetic field, the flux per Moiré unit cell is  $p/q\Phi_0$  where  $\Phi_0$  is the magnetic flux quantum. The continuum Hamiltonian for the  $K$  valley, con-

sidering the hole representation with unit charge  $+e$ , is given by

$$H_{\uparrow}(\mathbf{r}) = \begin{pmatrix} \frac{(\mathbf{p}-\hbar\boldsymbol{\kappa}_{+}-e\mathbf{A}(\mathbf{r}))^2}{2m^*} + \Delta_b(\mathbf{r}) & \Delta_T(\mathbf{r}) \\ \Delta_T^\dagger(\mathbf{r}) & \frac{(\mathbf{p}-\hbar\boldsymbol{\kappa}_{-}-e\mathbf{A}(\mathbf{r}))^2}{2m^*} + \Delta_t(\mathbf{r}) \end{pmatrix}. \quad (3.9)$$

Here, the vector potential  $\mathbf{A}$  is chosen in the modified Landau gauge Eq. (2.15) as

$$\mathbf{A} = \frac{p\hbar}{2\pi q} \mathbf{b}_2 \mathbf{b}_1 \cdot \mathbf{r}, \quad (3.10)$$

where Moiré reciprocal vectors  $\mathbf{b}_1 = \mathbf{G}_1$  and  $\mathbf{b}_2 = \mathbf{G}_3$ . By time-reversal symmetry, the Hamiltonian of the  $K'$  valley is

$$H_{\downarrow}(\mathbf{r}) = \begin{pmatrix} \frac{(\mathbf{p}-\hbar\boldsymbol{\kappa}_{+}+e\mathbf{A}(\mathbf{r}))^2}{2m^*} + \Delta_b(\mathbf{r}) & \Delta_T^\dagger(\mathbf{r}) \\ \Delta_T(\mathbf{r}) & \frac{(\mathbf{p}-\hbar\boldsymbol{\kappa}_{-}+e\mathbf{A}(\mathbf{r}))^2}{2m^*} + \Delta_t(\mathbf{r}) \end{pmatrix}. \quad (3.11)$$

To compute the Hofstadter spectrum, we apply generalized Bloch conditions that account for the magnetic flux per Moiré unit cell. By considering fractional magnetic fluxes  $\Phi = p/q\Phi_0$ , the resulting spectrum exhibits a fractal structure known as the Hofstadter butterfly. This spectrum is characterized by a series of energy levels and gaps corresponding to different rational flux values, as depicted in Fig. 3.3 for various twist angles  $\theta$ . The analysis of the Hofstadter spectra at different twist angles reveals several key features.

Across all twist angles, the Hofstadter spectrum indicates a valley-Zeeman effect. As the magnetic flux increases, the energy of the lowest band in the  $K$  valley decreases, while in the  $K'$  valley, it increases. This suggests that an external magnetic field induces valley polarization, reflecting a net orbital angular momentum effect even without spin-magnetic field coupling.

At small twist angles  $\theta = 1.2^\circ$ , the interaction between the lowest two bands is pronounced, leaving a large gap between them and the third band. This is due to the topological nature of the bands, where the sum of the Chern numbers of the bands below the gap

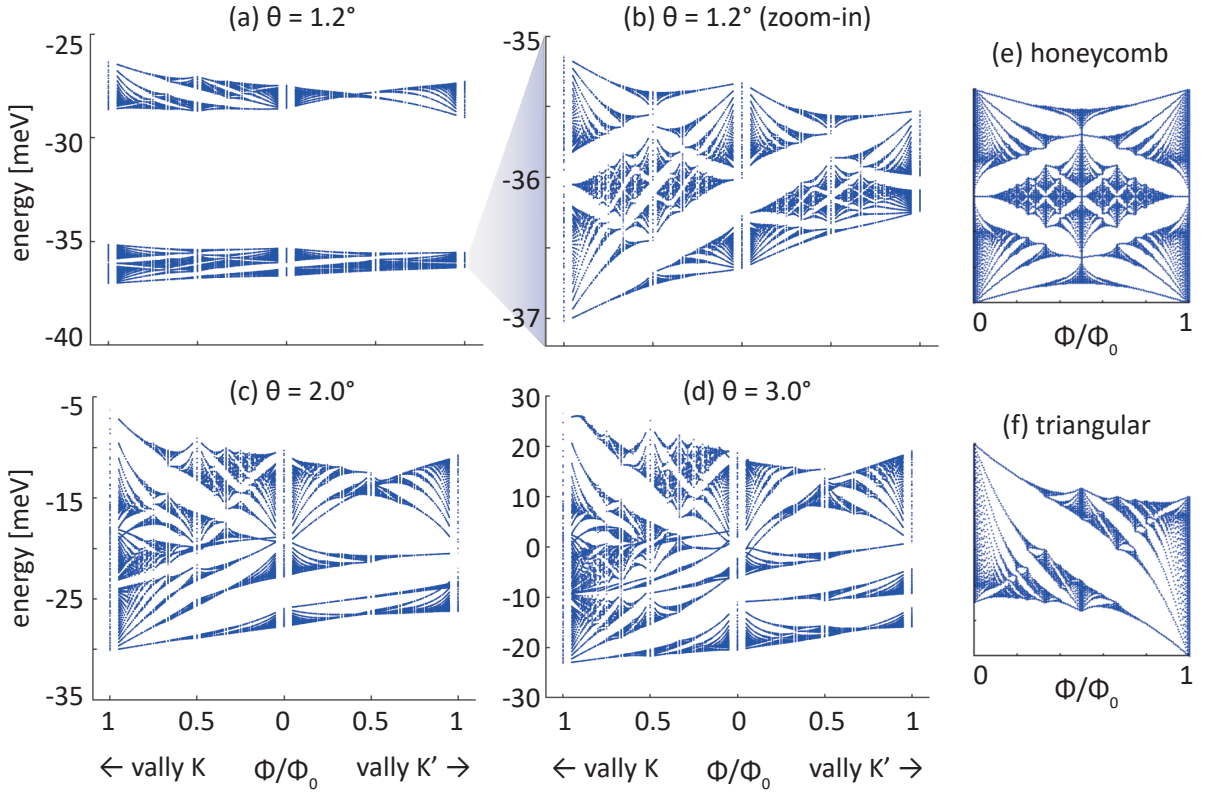


Figure 3.3: Hofstadter spectra of a  $\text{MoTe}_2$  homobilayer with twist angles: (a)  $\theta = 1.2^\circ$ , (c)  $\theta = 2.0^\circ$ , and (d)  $\theta = 3.0^\circ$ . Panel (b) shows a zoom-in of the spectrum in (a) at  $\theta = 1.2^\circ$ . For comparison, the Hofstadter spectra of the nearest-neighbor tight-binding model on (e) a honeycomb lattice and (f) a triangular lattice are also presented.

imposes an upper bound on the gap size. Since the Chern number of the lowest two bands is  $C = \pm 1$ , therefore the Hofstadter gap between them is topological and thus bounded, while the gap between the second band and the third band is topologically trivial and unbounded. The zoom-in spectrum of the lowest two bands is displayed in Fig. 3.4(b), which shares a similar pattern with the Hofstadter spectrum of the tight-binding model on a honeycomb lattice with nearest-neighbor hopping [Fig. 3.3(d)]. This similarity can be further illustrated by the spatial charge density of the lowest two bands, which resembles a honeycomb pattern. However, since the Dirac cones are gaped at  $\Phi = 0$ , the Hofstadter spectrum displays quantitatively different gap patterns.

At larger twist angles  $\theta = 2.0^\circ$  and  $3.0^\circ$ , the lowest three bands interact with each

other as the magnetic flux varies. This interaction is due to the Chern number bands:  $C = -1, -1, 2$ , respectively. The gaps between them are all topological and thus been bounded. The Hofstadter spectrum of the lowest band around  $\Phi = 0$  is partially similar to the triangular-lattice tight-binding model with nearest-neighbor hopping [Fig. 3.3(e)], since the charge density of the lowest band resembles a triangular lattice. Notably, near  $\Phi = \Phi_0$  at valley  $K$ , the Hofstadter spectrum exhibits a pronounced nearly-free-electron feature, where the slopes of the energy level are proportional to Landau levels  $n_{\text{LL}}$ . Together with the valley-Zeeman effect that energetically favors valley  $K$ , this feature implies a spontaneous composite fermion liquid phase at valley  $K$  with half-filling, which will be discussed in the next chapter.

### 3.4 Quantum Hall conductivity and Wannier's diagrams

In this section, we further investigate the topological properties of Moiré TMD systems by analyzing the quantum Hall conductivity and the corresponding Wannier's diagrams. The quantum Hall conductivity is a crucial indicator of the topological nature of the electronic bands in these systems. It provides direct insights into the quantization of Hall conductance, which is closely related to the Chern numbers of the Moiré bands. Recent studies have explored fractional quantum anomalous Hall states and transport properties in twisted bilayer systems [38], [39], and the role of flat Chern bands in proximity effects [40].

We calculate the quantum Hall conductivity by the Streda formula [41],

$$\sigma_{xy}(B, E_F) = e \frac{\partial \rho(E_F, B)}{\partial B}, \quad (3.12)$$

where  $\rho(E_F, B)$  is the cumulative energy density of state at Fermi-energy  $E_F$ . As shown in Fig. 3.4, the Hall conductivity is well quantized at gaps and aligns with the zero-field Chern numbers (Fig. 3.1). The gaps with larger Chern numbers are more tightly bounded, consistent with the gap-boundary theory. The non-trivial Chern numbers associated with the

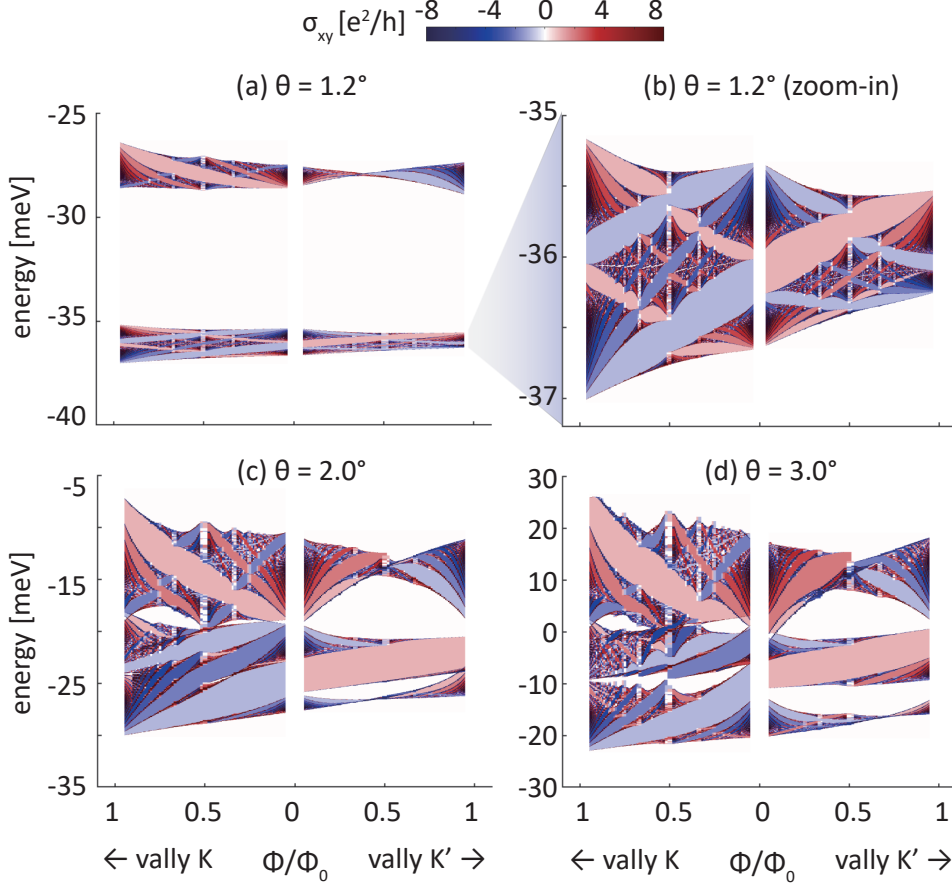


Figure 3.4: Hall conductivity of  $\text{MoTe}_2$  homobilayer with twist angle (a)(b)  $\theta = 1.2^\circ$ , (c)  $\theta = 2.0^\circ$ , and (d)  $\theta = 3.0^\circ$ , where (b) is a zoom-in of (a).

Moiré bands suggest that these systems can host a variety of quantum Hall effects, including the quantum anomalous Hall effect (QAHE) and potentially the fractional quantum Hall effect (FQHE) due to interaction. The flatness of the Moiré bands, combined with the Hofstadter spectrum, provides an ideal platform for exploring these topological phases and their associated quantum phenomena.

To further explore the intricate fractal nature of the Hofstadter spectrum, we employ the calculation of Wannier's diagram [42], a powerful tool for visualizing the relationship between magnetic flux and electron filling in the system. Wannier's diagram provides a graphical representation of the allowed energy gaps in the Hofstadter spectrum as a function of the magnetic flux per unit cell and the electron filling factor. This diagram is partic-

ularly insightful because it captures the topological properties of the system through the distribution and behavior of these energy gaps.

The foundation of Wannier's diagram lies in the Diophantine gap equation:

$$n/n_0 = t \frac{\Phi}{\Phi_0} + s, \quad (3.13)$$

where  $n/n_0$  is the electron filling factor, representing the ratio of the number of electrons per unit cell,  $t$  is the Chern number associated with the quantized Hall conductance, and  $s$  is another integer that corresponds to the gap index, effectively indicating the electron filling within the spectrum.

The Diophantine equation is crucial in understanding the quantization of Hall conductance in the Hofstadter butterfly. The Chern number  $t$  determines the topological nature of the bands and their contribution to the Hall conductance, while the integer  $s$  identifies specific energy gaps in the spectrum. These gaps are directly linked to incompressible quantum Hall states, which are of significant interest in both theoretical and experimental condensed matter physics.

The calculated Wannier's diagrams, the energy density of state as a function of filling factor  $n/n_0$  and magnetic flux  $\Phi$  as illustrated in Fig. 3.5, reveal the presence of these energy gaps across the spectrum. Each dark line in the diagram corresponds to an energy gap where the system exhibits an incompressible quantum Hall state, characterized by a quantized Hall conductance. The diagram not only provides a clear visualization of the gap structure but also offers insights into the topological phases that arise in Moiré TMD systems under varying magnetic flux conditions.

From an experimental perspective, Wannier's diagram can be directly linked to measurable quantities such as the electronic compressibility and quantum Hall conductance. These gaps, which are represented as dark lines in the diagram, correspond to regions of incompressibility in experimental measurements, where the electron density does not change

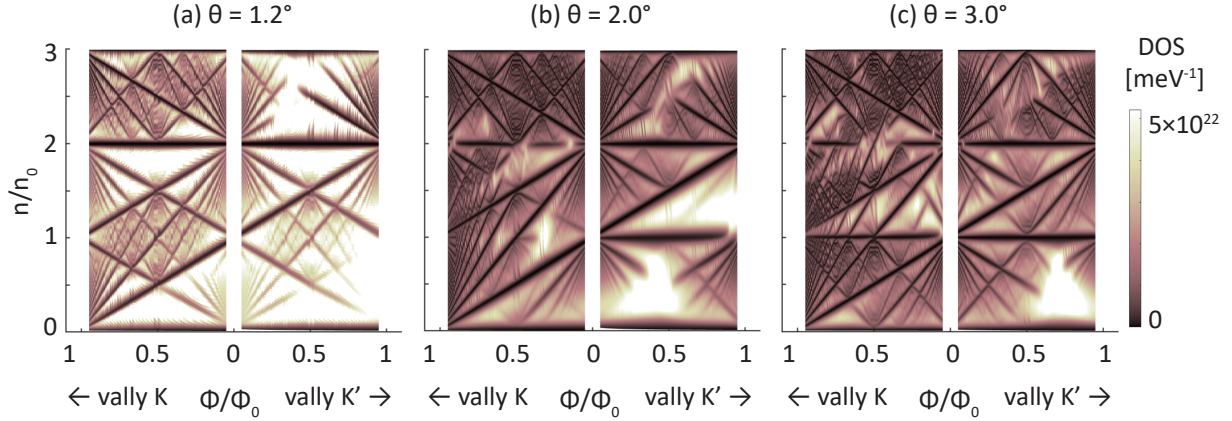


Figure 3.5: Wannier diagrams showing the energy density of states (DOS) for a MoTe<sub>2</sub> homobilayer at different twist angles: (a)  $\theta = 1.2^\circ$ , (b)  $\theta = 2.0^\circ$ , and (c)  $\theta = 3.0^\circ$ . The x-axis represents the magnetic flux per Moiré unit cell, while the y-axis indicates the filling factor, corresponding to the number of electrons per Moiré unit cell.

significantly with variations in chemical potential. Techniques like capacitance measurements or scanning probe microscopy can be employed to probe the compressibility of the electronic states, thereby indirectly measuring the gap structure of the Hofstadter spectrum.

### 3.5 Conclusion

In this chapter, we have explored the Hofstadter spectrum in Moiré TMD systems, highlighting the intricate interplay between the Moiré superlattice and an external magnetic field. By applying a continuum model and considering the effects of fractional magnetic fluxes, we have revealed the fractal nature of the Hofstadter butterfly and its associated energy gaps. The spectrum is rich with features, including the valley-Zeeman effect, the interaction between bands at various twist angles, and the emergence of topological quantum Hall states.

The Hofstadter spectrum provides profound insights into the quantum Hall effects and the topological properties of Moiré TMD. The application of Wannier's diagrams further enhances our understanding of the gap structure and its experimental implications. These findings suggest that Moiré TMD are promising platforms for exploring new quantum phases and could pave the way for future technological applications in topologically protected quan-

tum computing and high-precision metrology.

As we look ahead, the exploration of Hofstadter physics in other Moiré materials and the investigation of interaction-driven quantum phases in these systems hold great promise for advancing our understanding of condensed matter physics.



# Chapter 4

## Composite Fermions Mean-field Theory for Moiré Transition Metal Dichalcogenides

### 4.1 Introduction

Composite fermions are a cornerstone concept in the study of strongly correlated electron systems, particularly in the context of the fractional quantum Hall effect (FQHE). Introduced by Jain in 1989, the theory of composite fermions provides an elegant explanation for the observed FQHE by mapping the problem of interacting electrons in a strong magnetic field onto a problem of weakly interacting composite fermions in a reduced effective magnetic field (See Refs. [12], [13], [43], [44] for reviews).

Composite fermions are formed when electrons bind an even number of quantized vortices, effectively reducing the magnetic field experienced by these quasi-particles. This reduction transforms the complex many-body problem of interacting electrons into a more tractable problem of composite fermions filling Landau levels, known as  $\Lambda$  levels. The filling of these  $\Lambda$  levels leads to the formation of various quantum Hall states, characterized by fractional

filling factors, which correspond to the FQHE observed in experiments.

The success of the composite fermion model in explaining the FQHE has led to its application in various other systems, including those with Moiré superlattices. Theoretical advancements have shown that in Moiré systems, such as twisted bilayer graphene and transition metal dichalcogenides (TMD), the intricate interplay between strong correlations and Moiré potentials could lead to the emergence of composite fermion states. This motivates the extension of composite fermion theory to the study of Moiré TMD systems.

Recent experiments have provided strong evidence for zero-field fractional Chern insulators (FCIs) at fillings  $\nu = -2/3$  and  $-3/5$  in twisted bilayer MoTe<sub>2</sub> (tMoTe<sub>2</sub>) [6]. The  $\nu = -2/3$  FCI was also independently observed by Zeng et al. [7]. These experimental findings were anticipated by theoretical models of Chern bands in tMoTe<sub>2</sub> [37], as well as numerical studies that predicted FCIs at partial fillings in MoTe<sub>2</sub> [32] and WSe<sub>2</sub> [45], [46]. More recently, theoretical investigations combining ab-initio lattice relaxation and exact diagonalization on tMoTe<sub>2</sub> have also reported the presence of FCIs [38], [47].

Moiré TMD systems have garnered significant attention due to their unique ability to host FCI states, a form of the FQHE that can occur without the presence of an external magnetic field. This capability is one of the most fascinating aspects of TMD-based Moiré systems. The key to this phenomenon lies in the Berry curvature of the flat bands in TMD, which is relatively evenly distributed across the Brillouin zone. This distribution acts similarly to a magnetic field, facilitating the formation of FQHE states in the absence of an actual magnetic field.

The study of FCI states in Moiré TMD extends the concept of composite fermions into a new and intriguing regime, where the topological properties of the bands themselves, rather than an applied magnetic field, drive the formation of strongly correlated quantum states. In this chapter, our primary goal is to simulate the formation of FCI states using composite fermion mean-field theory, providing a theoretical framework for understanding how these exotic phases emerge in Moiré TMD systems.

This investigation is not only of theoretical significance but also holds promise for experimental realization. The tunability of Moiré superlattices via twist angle, external parameters, and electron density offers a versatile platform for probing the interplay between topology, strong correlations, and composite fermion physics. By simulating FCI states, we aim to uncover the potential quantum phases that could arise in these systems, further enriching the landscape of quantum materials.

## 4.2 Theoretical Framework

### 4.2.1 Jain's Composite Fermion Theory

The discovery of the fractional quantum Hall effect (FQHE) in the early 1980s posed a significant challenge to our understanding of many-body physics in two-dimensional electron systems subjected to strong magnetic fields. The FQHE occurs at fractional filling factors  $\nu = p/q$ , where  $p$  and  $q$  are integers, and it exhibits a quantized Hall conductance that is a fraction of the elementary quantum  $e^2/h$ . To explain this phenomenon, Jainendra Jain [13] proposed the theory of composite fermions, which has since become a cornerstone in the study of the FQHE.

Composite fermions are quasi-particles formed by attaching an even number of magnetic flux quanta,  $2\alpha\Phi_0$  (where  $\alpha$  is an integer and  $\Phi_0 = h/e$  is the magnetic flux quantum), to each electron. This flux attachment effectively transforms the strongly interacting electrons into weakly interacting composite fermions, which experience a reduced effective magnetic field

$$B^* = B - 2\alpha n_e \Phi_0, \quad (4.1)$$

where  $n_e$  is the electron density. In this reduced magnetic field, the composite fermions fill

up Landau levels just like non-interacting electrons, giving rise to an effective filling factor

$$\nu^* = \frac{n_e h}{e|B^*|}. \quad (4.2)$$

The observed fractional quantum Hall states correspond to integer quantum Hall states of composite fermions

$$\nu = \frac{\nu^*}{2\alpha\nu^* \pm 1} \quad (4.3)$$

where  $\nu^*$  is the integer filling factor of composite fermion Landau levels,  $\pm$  accounts for the sign of  $B^*$ . This mapping elegantly explains the FQHE as an integer quantum Hall effect of composite fermions. For example, when  $\alpha = 1$  and  $\nu^* = 1$ , we obtain the filling factor  $\nu = 1/3$ , corresponding to the first observed FQHE state. Similarly, other fractional filling factors can be derived, demonstrating the universality of Jain's composite fermion theory in describing the FQHE.

#### 4.2.2 Chern-Simons Field Theory and Flux Attachment

While Jain's theory provides a phenomenological explanation for the FQHE, a deeper understanding can be obtained by using Chern-Simons field theory [12], which formalizes the concept of flux attachment. In this framework, the attachment of flux quanta to electrons is described by introducing a Chern-Simons gauge field,  $a_\mu$ , into the system. The Chern-Simons Lagrangian is given by

$$\mathcal{L}_{\text{CS}} = \frac{\alpha}{4\pi} \epsilon^{\mu\nu\rho} a_\mu \partial_\nu a_\rho, \quad (4.4)$$

where  $\epsilon^{\mu\nu\rho}$  is the antisymmetric tensor, and  $\alpha$  is the number of flux quanta attached to each electron.

The key idea is that the gauge field  $a_\mu$  induces an effective magnetic field that cancels the

external magnetic field when averaged over the system, leading to the formation of composite fermions. These composite fermions experience the reduced magnetic field  $B^*$  and can fill Landau levels as discussed in Jain's theory.

The Chern-Simons field theory provides a robust mathematical framework to describe the formation of composite fermions and the resulting FQHE. It also allows for the inclusion of gauge field fluctuations, which can lead to corrections beyond the mean-field theory.

### 4.2.3 Composite Fermion Liquid Theory

At half-filled Landau levels, where  $\nu = 1/2$ , the situation becomes particularly intriguing. Here, the effective magnetic field  $B^*$  felt by the composite fermions is zero, suggesting that the composite fermions should form a Fermi liquid state. This idea was developed by Halperin, Lee, and Read (HLR) in their seminal theory of the composite fermion liquid [48].

In the HLR theory, the composite fermions at half-filling form a Fermi surface, similar to the Fermi surface in a conventional metal. The low-energy excitations around this Fermi surface behave like those of a Fermi liquid, but with additional interactions mediated by the Chern-Simons gauge field. These gauge field fluctuations lead to non-trivial corrections to the composite fermion's effective mass and other physical properties, distinguishing the composite fermion liquid from a conventional Fermi liquid.

The HLR theory has been instrumental in explaining various experimental observations at half-filling, such as the absence of the quantum Hall effect and the presence of metallic transport behavior. It also provides a framework for understanding the transition between the FQHE and the composite fermion liquid as the filling factor is varied.

### 4.2.4 Application to Moiré TMD Systems

Moiré TMD systems, with their flat bands and nontrivial topological properties, provide an ideal platform for exploring fractional Chern insulating (FCI) states. These states are the lattice analogs of the FQHE, but they can occur without an external magnetic field due to

the nonzero Berry curvature of the flat bands in these systems.

In a half-filled Moiré TMD system, the flatness of the bands and the even distribution of Berry curvature can lead to the formation of a composite fermion liquid state, analogous to the half-filled Landau level in the conventional FQHE. However, in this case, the composite fermions may form a Fermi surface in the absence of an external magnetic field, leading to an anomalous composite fermion liquid state [39].

The Chern-Simons theory can be applied to Moiré TMD to describe this state. By attaching flux quanta to the electrons in the flat bands, we can transform them into composite fermions, which then experience an effective magnetic field generated by the Berry curvature. The resulting state is a candidate for an anomalous composite fermion liquid, where the physics is governed by the interplay between the flat band, the Berry curvature, and the interactions between composite fermions.

In the next section, we will employ a mean-field theory to simulate this anomalous composite fermion liquid state in Moiré TMD, exploring its properties and potential experimental signatures. This approach will allow us to gain insights into the exotic quantum phases that can arise in these systems and their relevance to the broader field of topological quantum matter.

### 4.3 Composite Fermion Mean-field Theory in TMD

Building on the theoretical foundation established earlier, we now apply the concepts of composite fermions to Moiré TMD systems. Our goal is to explore the emergent phases in these systems, particularly focusing on the possibility of realizing a composite fermion liquid state without an external magnetic field.

In Moiré TMD systems, the flat bands with non-trivial Berry curvature create a unique environment where composite fermions could form a Fermi surface even without an external magnetic field. This state could manifest as a fractional Chern insulator (FCI), which is a

lattice analog of the fractional quantum Hall effect (FQHE) but occurring due to the intrinsic properties of the system rather than an applied magnetic field. To explore this possibility, we employ a mean-field theory approach to study the behavior of composite fermions in these materials.

The mean-field approximation simplifies the Hamiltonian by averaging the effects of the Chern-Simons gauge field, allowing us to treat the composite fermions as quasi-free particles. The Hamiltonian of the system (in the hole representation with unit charge  $+e$ ) is given by

$$H_{\uparrow}(\mathbf{r}) = \begin{pmatrix} \frac{(p - \hbar\kappa + e\mathbf{A}_{\text{MF}}(\mathbf{r}))^2}{2m^*} + \Delta_b(\mathbf{r}) & \Delta_T(\mathbf{r}) \\ \Delta_T^\dagger(\mathbf{r}) & \frac{(p - \hbar\kappa - e\mathbf{A}_{\text{MF}}(\mathbf{r}))^2}{2m^*} + \Delta_t(\mathbf{r}) \end{pmatrix}. \quad (4.5)$$

where  $\mathbf{A}_{\text{MF}}(\mathbf{r})$  is the mean-field vector potential, determined self-consistently by

$$\nabla \times \mathbf{A}_{\text{MF}}(\mathbf{r}) = \mathbf{B}_{\text{MF}}(\mathbf{r}) = \mathbf{B}_{\text{ext}} - 2\alpha\Phi_0 n(\mathbf{r})\hat{\mathbf{z}}. \quad (4.6)$$

Here,  $\mathbf{B}_{\text{ext}}$  represents the external uniform magnetic field,  $\alpha$  (an integer) is the number of flux quanta attached to each electron, and  $n(\mathbf{r})$  is the spatial density of electrons. The emergent magnetic field  $\mathbf{B}_{\text{MF}}(\mathbf{r})$  reflects both the external field and the contributions from the attached flux quanta, modulated by the electron density.

To further analyze the behavior of composite fermions under these conditions, we separate  $\mathbf{B}_{\text{MF}}$  into a spatially averaged part,  $\mathbf{B}_0 = \mathbf{B}_{\text{ext}} - 2\alpha\nu\Phi_0\hat{\mathbf{z}}/\mathcal{A}_{\text{cell}}$  with  $\nu$  the filling factor and  $\mathcal{A}_{\text{cell}}$  the area of unit cell, and the spatial various part,  $\mathbf{B}_{\text{var}}(\mathbf{r}) = 2\alpha\Phi_0\left(\frac{\nu}{\mathcal{A}_{\text{cell}}} - n(\mathbf{r})\right)\hat{\mathbf{z}}$ . The vector potential can be also split in the same way that  $\mathbf{A}_{\text{MF}} = \mathbf{A}_0 + \mathbf{A}_{\text{var}}(\mathbf{r})$ . The averaged part corresponds to a uniform effective magnetic field, while the varying part reflects local density fluctuations.

This separation enables the application of the plane-wave-based method to solve the self-consistent field (SCF) problem while preserving the periodicity imposed by the modified Landau gauge. Specifically, by choosing the modified Landau gauge as described in Eq. (2.15)

for  $\mathbf{A}_0$  with  $p/q\Phi_0$  representing the rational flux per unit cell of  $\mathbf{B}_0$ , the wave functions inherently satisfy the magnetic Bloch condition, as given by Eq. (2.16). If we assume that the electron density  $n(\mathbf{r})$  retains the same periodicity of the electron density  $n_0(\mathbf{r})$  with only the uniform component  $\mathbf{B}_0$  been considered, then spatially varying part  $\mathbf{B}_{\text{var}}(\mathbf{r})$  determined by  $n(\mathbf{r})$  averages to zero within each unit cell. As a result,  $\mathbf{A}_{\text{var}}(\mathbf{r})$  does not disrupt the magnetic Bloch condition established by  $\mathbf{A}_0$ . Consequently, the electron density  $n(\mathbf{r})$  is self-consistent with this periodic assumption, allowing us to directly apply the plane-wave-based method for the SCF problem without needing to modify the magnetic Bloch condition.

Now we will explicitly solve  $\mathbf{A}_{\text{var}}(\mathbf{r})$  from the electron density  $n(\mathbf{r})$ . Decomposing  $\mathbf{A}_{\text{var}}(\mathbf{r}) = (\mathbf{b}_1 \tilde{A}_{b_1}(\mathbf{r}) + \mathbf{b}_2 \tilde{A}_{b_2}(\mathbf{r}))\hbar/e$  where  $\tilde{A}_{b_1}$  and  $\tilde{A}_{b_2}$  are dimensionless, The curvature of  $\mathbf{A}_{\text{var}}(\mathbf{r})$  in fractional coordinates (defined in section 2.3) is then

$$\nabla \times \mathbf{A}_{\text{var}}(\mathbf{r}) = \frac{\Phi_0}{\mathcal{A}_{\text{cell}}} (\partial_{x_1} \tilde{A}_{b_2} - \partial_{x_2} \tilde{A}_{b_1}) \hat{\mathbf{z}}. \quad (4.7)$$

Using Fourier transformation with reciprocal lattice  $G_i \in 2\pi\mathbb{Z}$ ,

$$\tilde{A}_{b_i}(x_1, x_2) = \sum_{(G_1, G_2) \neq (0,0)} \tilde{A}_{G_1 G_2}^{(i)} e^{i(G_1 x_1 + G_2 x_2 / q)}, \quad (4.8)$$

$$n(x_1, x_2) = \frac{\nu}{\mathcal{A}_{\text{cell}}} + \sum_{(G_1, G_2) \neq (0,0)} n_{G_1 G_2} e^{i(G_1 x_1 + G_2 x_2 / q)}, \quad (4.9)$$

where the period of  $x_2$  is  $q$ -times enlarged in a magnet supercell, the Fourier components satisfy

$$iG_1 \tilde{A}_{G_1 G_2}^{(2)} - iG_2 \tilde{A}_{G_1 G_2}^{(1)}/q = 2\alpha \mathcal{A}_{\text{cell}} n_{G_1 G_2}. \quad (4.10)$$

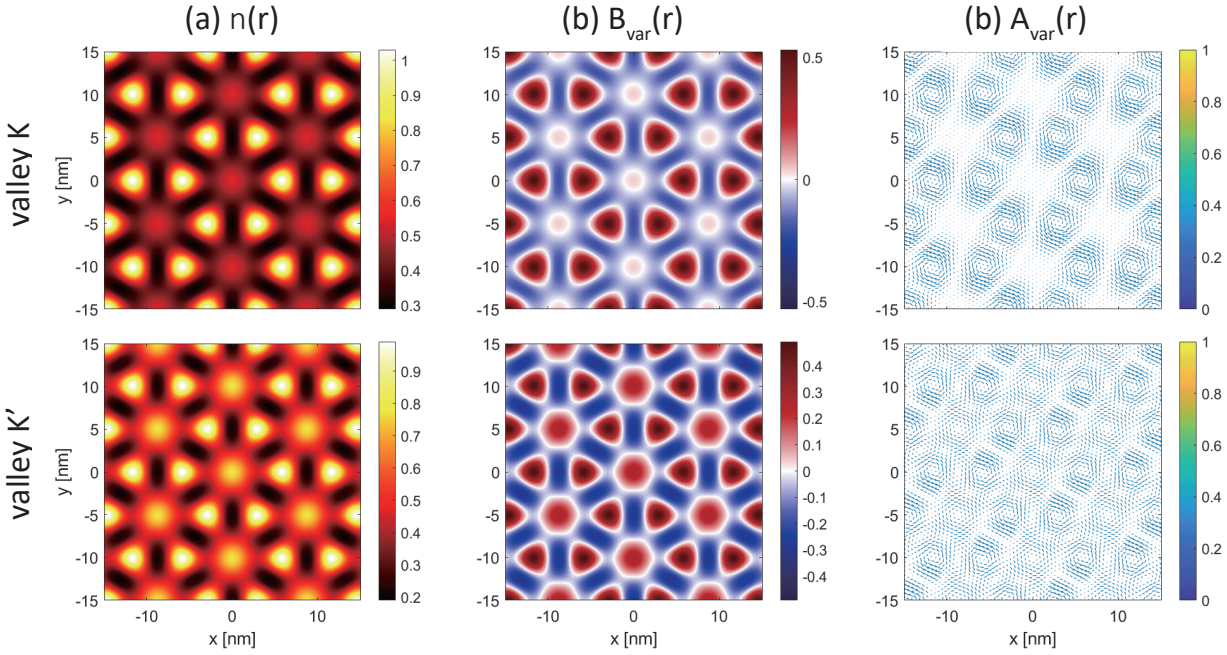


Figure 4.1: SCF solutions of twisted MoTe<sub>2</sub> homobilayer with twist angle  $\theta = 2.0^\circ$  at half-filling with  $2\Phi_0$  flux attachment per electron, where (a) is the charge density  $n(\mathbf{r})$ , (b) is  $B_{\text{var}}(\mathbf{r})$ , and (c) is  $\mathbf{A}_{\text{var}}(\mathbf{r})$ . The upper (lower) figures is calculated in valley  $K$  ( $K'$ ).

We choose the gauge of  $\mathbf{A}_{\text{var}}(\mathbf{r})$  such that  $iG_1\tilde{A}_{G_1G_2}^{(1)} + iG_2\tilde{A}_{G_1G_2}^{(2)}/q = 0$ , then

$$\begin{aligned}\tilde{A}_{G_1G_2}^{(1)} &= 2\alpha\mathcal{A}_{\text{cell}}n_{G_1G_2}\frac{iG_2/q}{G_1^2 + G_2^2}, \\ \tilde{A}_{G_1G_2}^{(2)} &= 2\alpha\mathcal{A}_{\text{cell}}n_{G_1G_2}\frac{-iG_1}{G_1^2 + G_2^2},\end{aligned}\tag{4.11}$$

where  $(G_1, G_2) \neq (0, 0)$ .  $\mathbf{A}_{\text{var}}(\mathbf{r})$  is explicitly determined by Eq. (4.11).

After solving  $\mathbf{A}_{\text{var}}(\mathbf{r})$ , the Hamiltonian  $H$  can be efficiently evaluated. We keep the definition of the mechanical momentum to be

$$\boldsymbol{\Pi} = \mathbf{p} + e\mathbf{A}_0,\tag{4.12}$$

where only the spatial average part  $\mathbf{A}_0$  is included. It can be decomposed to  $\boldsymbol{\Pi} = \hbar\mathbf{b}_1\tilde{\Pi}_1 + \hbar\mathbf{b}_2\tilde{\Pi}_2$  where  $\tilde{\Pi}_1$  and  $\tilde{\Pi}_2$  satisfy Eq. (2.23). Expressing  $\mathbf{A}_{\text{var}} = (\tilde{A}_{a_1}\hat{\mathbf{a}}_1/a_1 + \tilde{A}_{a_2}\hat{\mathbf{a}}_2/a_2)\hbar/(2\pi e)$

with relationship

$$\tilde{A}_{a_1} = a_1^2(\tilde{A}_{b_1}b_1^2 + \tilde{A}_{b_2}\mathbf{b}_1 \cdot \mathbf{b}_2), \quad (4.13)$$

$$\tilde{A}_{a_2} = a_2^2(\tilde{A}_{b_2}b_2^2 + \tilde{A}_{b_1}\mathbf{b}_1 \cdot \mathbf{b}_2), \quad (4.14)$$

the Hamiltonian is simplified to

$$H = \frac{1}{2m}\boldsymbol{\Pi}^2 + V + \frac{\hbar^2}{2ma_1^2}\{\tilde{A}_{a_1}, \tilde{\Pi}_1\} + \frac{\hbar^2}{2ma_2^2}\{\tilde{A}_{a_2}, \tilde{\Pi}_2\} + \frac{e^2}{2m}\mathbf{A}_{\text{var}}^2. \quad (4.15)$$

A SCF solutions of twisted MoTe<sub>2</sub> homobilayer is presented in Fig. 4.1.

In the following section, we will present the numerical results obtained using this framework, offering insights into the exotic quantum phases that may arise in Moiré TMD systems.

## 4.4 Mean-field Evidence for Anomalous Composite Fermion Liquid State

In this section, we present a detailed mean-field analysis that supports the potential existence of an anomalous composite fermion liquid state in Moiré TMD systems. Our investigation focuses on simulating the behavior of composite fermions and comparing their properties with those of the standard electronic configuration. The results suggest that Moiré TMD could be strong candidates for realizing such an anomalous state at half-filling, characterized by distinct valley polarization.

To simulate the composite fermion state in Moiré TMD, we begin by considering the system at half-filling. We assumed fully polarized valley, either  $K$  or  $K'$ . Each electron is modeled as being attached to two flux quanta, corresponding to  $\alpha = 1$  in the composite fermion theory. The system is considered in the absence of an external magnetic field ( $B_{\text{ext}} = 0$ ). Despite the absence of an external field, the composite fermion picture results in an

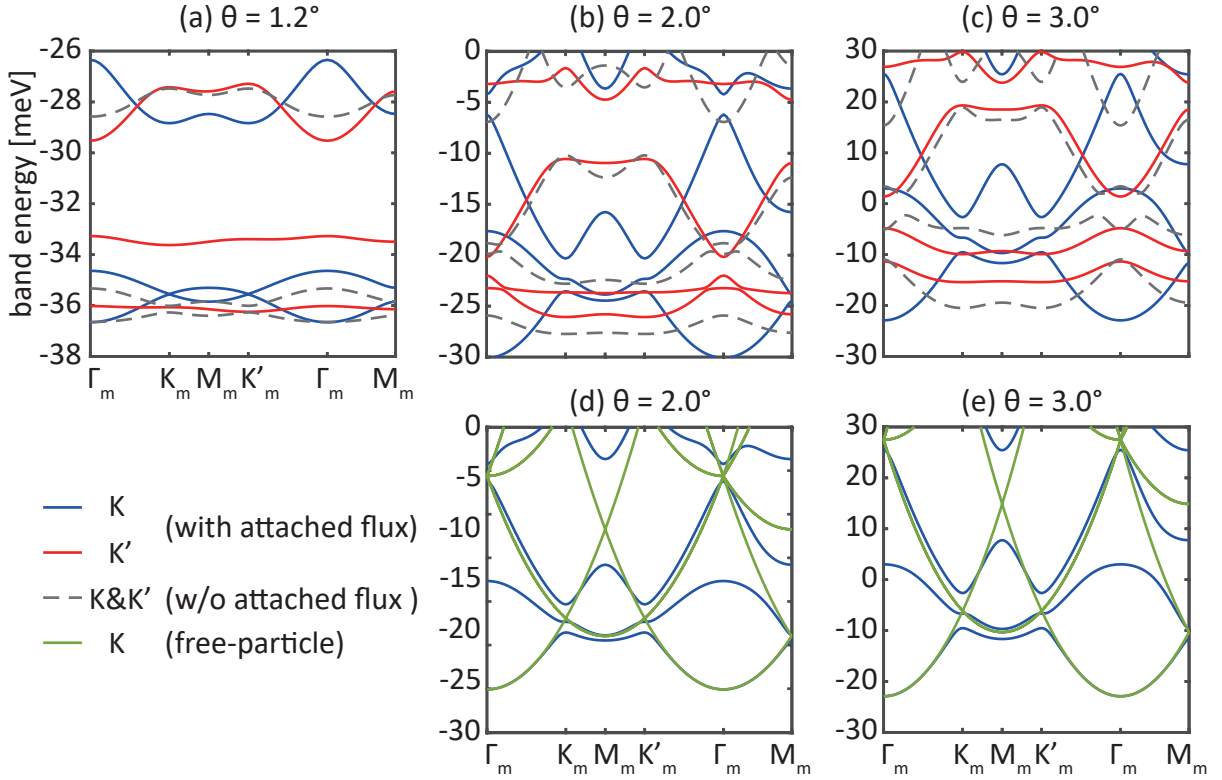


Figure 4.2: Mean-field band structures of a twisted MoTe<sub>2</sub> homobilayer at twist angles: (a)  $\theta = 1.2^\circ$ , (b)  $\theta = 2.0^\circ$ , and (c)  $\theta = 3.0^\circ$ . The blue and red lines represent composite fermions with a flux attachment of  $2\Phi_0$  per electron in valleys  $K$  and  $K'$ , respectively, while the gray dashed lines indicate the band structures of bare electrons without flux attachment in either valley. Panels (d) and (e) provide a comparison to the free-particle limit (green lines) for valleys  $K$  at twist angles  $\theta = 2.0^\circ$  and  $\theta = 3.0^\circ$ , respectively.

effective magnetic flux per unit cell that averaged to  $\Phi_0$ , due to the intrinsic flux attachment.

We first compare the band structures in the  $K$  valley under two scenarios: with and without flux attachment. The calculated band structures are presented in Fig. 4.2. The most notable differences are observed at twist angles  $\theta = 2.0^\circ$  and  $\theta = 3.0^\circ$ . In these cases, the lowest band in the  $K$  valley with flux attachment displays a pronounced parabolic dispersion around band bottom, which is a hallmark of nearly-free-particle behavior, which is clearly seen in Fig. 4.2 (d) and (e). The fitted effective masses are  $m^*/m = 1.30$  at  $\theta = 2.0$  and  $m^*/m = 1.42$  at  $\theta = 2.0$ . In addition, the lowest two bands in the  $K$  valley with flux attachment at  $\theta = 1.2^\circ$  exhibit gapless Dirac cones, indicating nearly-free Dirac fermion

	with flux attachment		without flux attachment		
$\theta$	$E_F$	$E_{\text{tot}}$	$E_F$	$E_{\text{tot}}$	$\Delta E_{\text{tot}}$
$1.2^\circ$	-36.0554	-18.1458	-36.4619	-18.2571	0.1113
$2.0^\circ$	-26.7749	-14.2364	-27.4550	-13.7872	-0.4492
$3.0^\circ$	-15.9994	-9.66593	-18.7454	-9.84835	0.1824

Table 4.1: The energy comparison between composite-fermi sea (with  $\Phi_0$  flux attachment) and bare electron fermi sea (without flux attachment) in valley  $K$  at half-filling, where  $E_F$  is Fermi energy,  $E_{\text{tot}}$  is the total energy per unit cell, and  $\Delta E_{\text{tot}}$  is the difference of  $E_{\text{tot}}$  between composite-fermi sea and bare electron fermi sea. All energies are in units of meV.

behavior. Furthermore, the band energy around these band bottoms is lower comparing to band bottoms without flux attachment at  $\theta = 2.0^\circ$  and  $\theta = 3.0^\circ$ , suggesting a more energetically favored ground state. In contrast, the bands in the  $K'$  valley remain relatively flat comparing to those without flux attachment with higher band energy. This difference in the response between the two valleys points to a possible valley polarization, where the composite fermion liquid state may preferentially form in the  $K$  valley.

To further investigate the stability and preference of the composite fermion liquid state, we compare the total energy per Moiré unit cell  $E_{\text{tot}}$  and the Fermi energy  $E_F$  in the  $K$  valley for scenarios with and without flux attachment, as shown in Tab. 4.1. The results indicate that at twist angles  $\theta = 2.0^\circ$ , the total energy of the composite fermion liquid state in the  $K$  valley is lower than that of the non-flux-attached state. This energy difference suggests that the system energetically favors the formation of a composite fermion liquid state at the  $K$  valley.

The mean-field analysis presented in this section provides compelling evidence for the existence of an anomalous composite fermion liquid state in Moiré TMD systems, particularly around twist angles  $\theta = 2.0^\circ$  and in the presence of valley polarization. The band structure analysis reveals a nearly-free-particle behavior in the  $K$  valley when flux quanta are attached, while the energy comparison underscores the energetic favorability of this state under certain conditions. These findings suggest that Moiré TMD are promising candidates for hosting novel quantum phases, such as a valley-polarized composite fermion liquid state, which could

be further explored in experimental settings.

## 4.5 Discussion

Building on the mean-field evidence presented in the previous section, which suggests the existence of an anomalous composite fermion liquid state in Moiré TMD systems, we further explore the theoretical framework underpinning this state. The mean-field simulations showed that at certain twist angles, particularly around  $\theta = 2.0^\circ$ , the composite fermion phase demonstrates a stable Fermi liquid behavior with a lower energy state compared to the standard electronic configuration. This stability, marked by distinct valley polarization and effective flux attachment, highlights the unique transport properties of composite fermions in a half-filled Chern band. These properties include a Hall resistivity close to  $2h/e$  and a gapped plasmon mode, features that are not observed in traditional FQHE systems but are characteristic of the intrinsic Berry curvature in Chern bands [39].

Our findings suggest that the composite fermion liquid state is not only energetically favorable but also capable of undergoing a phase transition influenced by changes in interaction strength or external parameters, such as the displacement field. This phase transition, characterized by an increase in longitudinal resistivity, aligns with experimental observations in twisted bilayer MoTe<sub>2</sub>, where the composite fermion phase could emerge under specific conditions. Thus, our simulations provide valuable insights into the complex interplay between band structure, Berry curvature, and transport phenomena in topologically nontrivial systems, reinforcing the potential of Moiré TMD as a platform for exploring novel quantum phases, including the valley-polarized composite fermion liquid state.



# Chapter 5

## Conclusions and Future Work

### 5.1 Conclusions

This thesis has explored the rich and complex physics of Moiré transition metal dichalcogenides (TMD), focusing on their potential to host novel quantum phases of matter, such as fractional quantum Hall effect (FQHE) and composite fermion liquid states, in the absence of external magnetic fields. The research conducted within these pages has demonstrated the unique interplay between the Moiré superlattice and magnetic fields, which leads to the emergence of fascinating quantum phenomena.

In chapter. 2, we began by discussing the foundational concepts of electronic structures in periodic potentials and external magnetic fields, laying the groundwork for understanding the behavior of electrons in TMD systems. We detailed the formation of Landau levels and the importance of generalized Bloch conditions in determining the electronic properties of these systems, and developed continuum-space numerical algorithms to solve the system.

Chapter. 3 focused on the Hofstadter physics in twisted bilayer TMD, where the Moiré superlattice gives rise to a rich Hofstadter spectrum when subjected to a magnetic field. The detailed analysis revealed key features of the spectrum, including the valley-Zeeman effect and the interaction between bands at various twist angles. The study also demonstrated that

the quantum Hall conductivity in these systems is deeply tied to the underlying topological properties of the Moiré bands.

Chapter. 4 extended the investigation into the realm of composite fermions, introducing composite fermion theory and applying it to Moiré TMD systems. We demonstrated that at half-filling, the system could support an anomalous composite fermion liquid state, with strong valley polarization, even in the absence of an external magnetic field. The mean-field analysis presented in this chapter provided compelling evidence for this state, showing that it is energetically favorable under certain conditions. This suggests that Moiré TMD could be an ideal platform for exploring new quantum phases, such as fractional Chern insulators (FCI), and potentially lead to groundbreaking developments in topological quantum computing.

Overall, the work presented in this thesis highlights the versatility and potential of Moiré TMD as a playground for discovering and understanding novel quantum phases. The interplay between strong electron correlations, topological properties, and Moiré engineering opens up a vast landscape of possibilities for future research.

## 5.2 Future Work

The findings of this thesis pave the way for several exciting avenues of future research. One of the most immediate directions is the experimental realization and characterization of the predicted anomalous composite fermion liquid state in Moiré TMD systems. High-resolution angle-resolved photoemission spectroscopy (ARPES) and scanning tunneling microscopy (STM) could be employed to probe the band structures and electronic states predicted by our theoretical models. Such experiments would be crucial in validating the mean-field results and further refining the theoretical framework.

Another promising direction is the study of interaction effects beyond the mean-field approximation. While the mean-field theory has provided valuable insights, the inclusion

of fluctuations and correlations could reveal even richer physics, particularly in the regime of strong coupling where exotic phases like non-Abelian anyons or fractionalized excitations might emerge. Numerical techniques such as density matrix renormalization group (DMRG) or quantum Monte Carlo (QMC) simulations could be employed to explore these possibilities.

Furthermore, the potential of Moiré TMD as a platform for topologically protected quantum computing should be thoroughly investigated. The interplay between the composite fermion liquid state and topological qubits, particularly in the context of fault-tolerant quantum computation, could lead to novel approaches for building quantum computers that are robust against decoherence and operational errors.

Lastly, extending the study of Moiré systems to other 2D materials beyond TMD could uncover new quantum phases and broaden our understanding of Moiré physics. Materials such as twisted bilayer graphene or hybrid heterostructures combining different 2D materials could exhibit distinct electronic properties that challenge and expand the current theoretical paradigms.

In conclusion, the exploration of Moiré TMD systems is still in its early stages, with much left to be discovered. The work presented in this thesis has laid a solid foundation, but the journey to fully understand and harness the potential of these fascinating materials is just beginning.



# References

- [1] E. Y. Andrei, D. K. Efetov, P. Jarillo-Herrero, A. H. MacDonald, K. F. Mak, T. Senthil, E. Tutuc, A. Yazdani, and A. F. Young, “The marvels of moiré materials,” *Nature Reviews Materials*, vol. 6, no. 3, pp. 201–206, Mar. 2021. DOI: [10.1038/s41578-021-00284-1](https://doi.org/10.1038/s41578-021-00284-1). URL: <https://doi.org/10.1038/s41578-021-00284-1>.
- [2] Y. Cao, V. Fatemi, S. Fang, K. Watanabe, T. Taniguchi, E. Kaxiras, and P. Jarillo-Herrero, “Unconventional superconductivity in magic-angle graphene superlattices,” *Nature*, vol. 556, no. 7699, pp. 43–50, Apr. 2018. DOI: [10.1038/nature26160](https://doi.org/10.1038/nature26160). URL: <https://doi.org/10.1038/nature26160>.
- [3] X. Lu, P. Stepanov, W. Yang, *et al.*, “Superconductors, orbital magnets and correlated states in magic-angle bilayer graphene,” *Nature*, vol. 574, no. 7780, pp. 653–657, Oct. 2019. DOI: [10.1038/s41586-019-1695-0](https://doi.org/10.1038/s41586-019-1695-0). URL: <https://doi.org/10.1038/s41586-019-1695-0>.
- [4] Y. Jiang, X. Lai, K. Watanabe, T. Taniguchi, K. Haule, J. Mao, and E. Y. Andrei, “Charge order and broken rotational symmetry in magic-angle twisted bilayer graphene,” *Nature*, vol. 573, no. 7772, pp. 91–95, Sep. 2019. DOI: [10.1038/s41586-019-1460-4](https://doi.org/10.1038/s41586-019-1460-4). URL: <https://doi.org/10.1038/s41586-019-1460-4>.
- [5] Y. Xie, A. T. Pierce, J. M. Park, *et al.*, “Fractional chern insulators in magic-angle twisted bilayer graphene,” *Nature*, vol. 600, no. 7889, pp. 439–443, Dec. 2021. DOI: [10.1038/s41586-021-04002-3](https://doi.org/10.1038/s41586-021-04002-3). URL: <https://doi.org/10.1038/s41586-021-04002-3>.

- [6] J. Cai, E. Anderson, C. Wang, *et al.*, “Signatures of fractional quantum anomalous hall states in twisted mote2,” *Nature*, vol. 622, no. 7981, pp. 63–68, Oct. 2023. DOI: [10.1038/s41586-023-06289-w](https://doi.org/10.1038/s41586-023-06289-w). URL: <https://doi.org/10.1038/s41586-023-06289-w>.
- [7] Y. Zeng, Z. Xia, K. Kang, J. Zhu, P. Knüppel, C. Vaswani, K. Watanabe, T. Taniguchi, K. F. Mak, and J. Shan, “Thermodynamic evidence of fractional chern insulator in moiré mote2,” *Nature*, vol. 622, no. 7981, pp. 69–73, Oct. 2023. DOI: [10.1038/s41586-023-06452-3](https://doi.org/10.1038/s41586-023-06452-3). URL: <https://doi.org/10.1038/s41586-023-06452-3>.
- [8] C. R. Dean, L. Wang, P. Maher, *et al.*, *Hofstadter’s butterfly and the fractal quantum hall effect in moiré superlattices*, May 2013. DOI: [10.1038/nature12186](https://doi.org/10.1038/nature12186). URL: <https://www.nature.com/articles/nature12186>.
- [9] B. Hunt, J. D. Sanchez-Yamagishi, A. F. Young, *et al.*, “Massive dirac fermions and hofstadter butterfly in a van der waals heterostructure,” *Science*, vol. 340, no. 6139, pp. 1427–1430, 2013. DOI: [10.1126/science.1237240](https://doi.org/10.1126/science.1237240). URL: <https://www.science.org/doi/abs/10.1126/science.1237240>.
- [10] X. Lu, B. Lian, G. Chaudhary, *et al.*, “Multiple flat bands and topological hofstadter butterfly in twisted bilayer graphene close to the second magic angle,” *Proceedings of the National Academy of Sciences*, vol. 118, no. 30, e2100006118, 2021. DOI: [10.1073/pnas.2100006118](https://doi.org/10.1073/pnas.2100006118). eprint: <https://www.pnas.org/doi/pdf/10.1073/pnas.2100006118>. URL: <https://www.pnas.org/doi/abs/10.1073/pnas.2100006118>.
- [11] D. J. Thouless, M. Kohmoto, M. P. Nightingale, and M. den Nijs, “Quantized hall conductance in a two-dimensional periodic potential,” *Phys. Rev. Lett.*, vol. 49, pp. 405–408, 6 Aug. 1982. DOI: [10.1103/PhysRevLett.49.405](https://doi.org/10.1103/PhysRevLett.49.405). URL: <https://link.aps.org/doi/10.1103/PhysRevLett.49.405>.
- [12] B. I. Halperin, “Fermion chern-simons theory and the unquantized quantum hall effect,” 2007. URL: <https://api.semanticscholar.org/CorpusID:117563026>.

- [13] J. K. Jain, “Composite-fermion approach for the fractional quantum hall effect,” *Phys. Rev. Lett.*, vol. 63, pp. 199–202, 2 Jul. 1989. DOI: [10.1103/PhysRevLett.63.199](https://doi.org/10.1103/PhysRevLett.63.199). URL: <https://link.aps.org/doi/10.1103/PhysRevLett.63.199>.
- [14] D. R. Hofstadter, “Energy levels and wave functions of bloch electrons in rational and irrational magnetic fields,” *Phys. Rev. B*, vol. 14, pp. 2239–2249, 6 Sep. 1976. DOI: [10.1103/PhysRevB.14.2239](https://doi.org/10.1103/PhysRevB.14.2239). URL: <https://link.aps.org/doi/10.1103/PhysRevB.14.2239>.
- [15] A. Kol and N. Read, “Fractional quantum hall effect in a periodic potential,” *Phys. Rev. B*, vol. 48, pp. 8890–8898, 12 Sep. 1993. DOI: [10.1103/PhysRevB.48.8890](https://doi.org/10.1103/PhysRevB.48.8890). URL: <https://link.aps.org/doi/10.1103/PhysRevB.48.8890>.
- [16] L. Landau, “Diamagnetismus der metalle,” *Zeitschrift für Physik*, vol. 64, no. 9, pp. 629–637, Sep. 1930. DOI: [10.1007/BF01397213](https://doi.org/10.1007/BF01397213). URL: <https://doi.org/10.1007/BF01397213>.
- [17] E. Brown, “Bloch electrons in a uniform magnetic field,” *Phys. Rev.*, vol. 133, A1038–A1044, 4A Feb. 1964. DOI: [10.1103/PhysRev.133.A1038](https://doi.org/10.1103/PhysRev.133.A1038). URL: <https://link.aps.org/doi/10.1103/PhysRev.133.A1038>.
- [18] J. Zak, “Magnetic translation group. ii. irreducible representations,” *Phys. Rev.*, vol. 134, A1607–A1611, 6A Jun. 1964. DOI: [10.1103/PhysRev.134.A1607](https://doi.org/10.1103/PhysRev.134.A1607). URL: <https://link.aps.org/doi/10.1103/PhysRev.134.A1607>.
- [19] H. J. Fischbeck, “Theory of bloch electrons in a magnetic field,” *physica status solidi (b)*, vol. 38, no. 1, pp. 11–62, 1970. DOI: <https://doi.org/10.1002/pssb.19700380102>. eprint: <https://onlinelibrary.wiley.com/doi/pdf/10.1002/pssb.19700380102>. URL: <https://onlinelibrary.wiley.com/doi/abs/10.1002/pssb.19700380102>.
- [20] E. Lee, W. Cai, and G. A. Galli, “Electronic structure calculations in a uniform magnetic field using periodic supercells,” *Journal of Computational Physics*, vol. 226, no. 2, pp. 1310–1331, 2007, ISSN: 0021-9991. DOI: <https://doi.org/10.1016/j.jcp.2007.05.022>. URL: <https://www.sciencedirect.com/science/article/pii/S0021999107002355>.

- [21] W. Cai and G. Galli, “Ab initio calculations in a uniform magnetic field using periodic supercells,” *Phys. Rev. Lett.*, vol. 92, p. 186402, 18 May 2004. DOI: [10.1103/PhysRevLett.92.186402](https://doi.org/10.1103/PhysRevLett.92.186402). URL: <https://link.aps.org/doi/10.1103/PhysRevLett.92.186402>.
- [22] M. P. Teter, M. C. Payne, and D. C. Allan, “Solution of schrödinger’s equation for large systems,” *Phys. Rev. B*, vol. 40, pp. 12 255–12 263, 18 Dec. 1989. DOI: [10.1103/PhysRevB.40.12255](https://doi.org/10.1103/PhysRevB.40.12255). URL: <https://link.aps.org/doi/10.1103/PhysRevB.40.12255>.
- [23] G. Kresse and J. Furthmüller, “Efficient iterative schemes for ab initio total-energy calculations using a plane-wave basis set,” *Phys. Rev. B*, vol. 54, pp. 11 169–11 186, 16 Oct. 1996. DOI: [10.1103/PhysRevB.54.11169](https://doi.org/10.1103/PhysRevB.54.11169). URL: <https://link.aps.org/doi/10.1103/PhysRevB.54.11169>.
- [24] M. Aichinger, S. Chin, and E. Krotscheck, “Fourth-order algorithms for solving local schrödinger equations in a strong magnetic field,” *Computer Physics Communications*, vol. 171, no. 3, pp. 197–207, 2005, ISSN: 0010-4655. DOI: <https://doi.org/10.1016/j.cpc.2005.05.006>. URL: <https://www.sciencedirect.com/science/article/pii/S0010465505003115>.
- [25] S. A. Chin, S. Janecek, and E. Krotscheck, “Any order imaginary time propagation method for solving the schrödinger equation,” *Chemical Physics Letters*, vol. 470, no. 4, pp. 342–346, 2009, ISSN: 0009-2614. DOI: <https://doi.org/10.1016/j.cplett.2009.01.068>. URL: <https://www.sciencedirect.com/science/article/pii/S0009261409001080>.
- [26] S. Janecek, M. Aichinger, and E. R. Hernández, “Two-dimensional bloch electrons in perpendicular magnetic fields: An exact calculation of the hofstadter butterfly spectrum,” *Phys. Rev. B*, vol. 87, p. 235429, 23 Jun. 2013. DOI: [10.1103/PhysRevB.87.235429](https://doi.org/10.1103/PhysRevB.87.235429). URL: <https://link.aps.org/doi/10.1103/PhysRevB.87.235429>.

- [27] R. Bistritzer and A. H. MacDonald, “Moiré butterflies in twisted bilayer graphene,” *Phys. Rev. B*, vol. 84, p. 035440, 3 Jul. 2011. DOI: [10.1103/PhysRevB.84.035440](https://doi.org/10.1103/PhysRevB.84.035440). URL: <https://link.aps.org/doi/10.1103/PhysRevB.84.035440>.
- [28] M. Wilkinson, “Critical properties of electron eigenstates in incommensurate systems,” *Proc. R. Soc. Lond. A*, vol. 391, pp. 305–350, 1984. DOI: <http://doi.org/10.1098/rspa.1984.0016>. URL: <https://dx.doi.org/10.1088/0370-1298/68/10/304>.
- [29] P. G. Harper, “Single band motion of conduction electrons in a uniform magnetic field,” *Proceedings of the Physical Society. Section A*, vol. 68, no. 10, p. 874, Oct. 1955. DOI: [10.1088/0370-1298/68/10/304](https://doi.org/10.1088/0370-1298/68/10/304). URL: <https://dx.doi.org/10.1088/0370-1298/68/10/304>.
- [30] C. Forsythe, X. Zhou, K. Watanabe, T. Taniguchi, A. Pasupathy, P. Moon, M. Koshino, P. Kim, and C. R. Dean, “Band structure engineering of 2d materials using patterned dielectric superlattices,” *Nature Nanotechnology*, vol. 13, no. 7, pp. 566–571, Jul. 2018. DOI: [10.1038/s41565-018-0138-7](https://doi.org/10.1038/s41565-018-0138-7). URL: <https://doi.org/10.1038/s41565-018-0138-7>.
- [31] R. Huber, M.-H. Liu, S.-C. Chen, M. Drienovsky, A. Sandner, K. Watanabe, T. Taniguchi, K. Richter, D. Weiss, and J. Eroms, “Gate-tunable two-dimensional superlattices in graphene,” *Nano Letters*, vol. 20, no. 11, pp. 8046–8052, Nov. 2020. DOI: [10.1021/acs.nanolett.0c03021](https://doi.org/10.1021/acs.nanolett.0c03021). URL: <https://doi.org/10.1021/acs.nanolett.0c03021>.
- [32] H. Li, U. Kumar, K. Sun, and S.-Z. Lin, “Spontaneous fractional chern insulators in transition metal dichalcogenide moiré superlattices,” *Phys. Rev. Res.*, vol. 3, p. L032070, 3 Sep. 2021. DOI: [10.1103/PhysRevResearch.3.L032070](https://doi.org/10.1103/PhysRevResearch.3.L032070). URL: <https://link.aps.org/doi/10.1103/PhysRevResearch.3.L032070>.
- [33] E. M. Spanton, A. A. Zibrov, H. Zhou, T. Taniguchi, K. Watanabe, M. P. Zaletel, and A. F. Young, “Observation of fractional chern insulators in a van der waals heterostructure,” *Science*, vol. 360, no. 6384, pp. 62–66, 2018. DOI: [10.1126/science.aan8458](https://doi.org/10.1126/science.aan8458). URL: <https://www.science.org/doi/abs/10.1126/science.aan8458>.

- [34] K. Hejazi, C. Liu, and L. Balents, “Landau levels in twisted bilayer graphene and semiclassical orbits,” *Phys. Rev. B*, vol. 100, p. 035115, 3 Jul. 2019. DOI: [10.1103/PhysRevB.100.035115](https://doi.org/10.1103/PhysRevB.100.035115). URL: <https://link.aps.org/doi/10.1103/PhysRevB.100.035115>.
- [35] B. Andrews and A. Soluyanov, “Fractional quantum hall states for moiré superstructures in the hofstadter regime,” *Phys. Rev. B*, vol. 101, p. 235312, 23 Jun. 2020. DOI: [10.1103/PhysRevB.101.235312](https://doi.org/10.1103/PhysRevB.101.235312). URL: <https://link.aps.org/doi/10.1103/PhysRevB.101.235312>.
- [36] Y. Okada, W. Zhou, C. Dhital, D. Walkup, Y. Ran, Z. Wang, S. D. Wilson, and V. Madhavan, “Visualizing landau levels of dirac electrons in a one-dimensional potential,” *Phys. Rev. Lett.*, vol. 109, p. 166407, 16 Oct. 2012. DOI: [10.1103/PhysRevLett.109.166407](https://doi.org/10.1103/PhysRevLett.109.166407). URL: <https://link.aps.org/doi/10.1103/PhysRevLett.109.166407>.
- [37] F. Wu, T. Lovorn, E. Tutuc, I. Martin, and A. H. MacDonald, “Topological insulators in twisted transition metal dichalcogenide homobilayers,” *Phys. Rev. Lett.*, vol. 122, p. 086402, 8 Feb. 2019. DOI: [10.1103/PhysRevLett.122.086402](https://doi.org/10.1103/PhysRevLett.122.086402). URL: <https://link.aps.org/doi/10.1103/PhysRevLett.122.086402>.
- [38] A. P. Reddy, F. Alsallom, Y. Zhang, T. Devakul, and L. Fu, “Fractional quantum anomalous hall states in twisted bilayer MoTe<sub>2</sub> and WSe<sub>2</sub>,” *Phys. Rev. B*, vol. 108, p. 085117, 8 Aug. 2023. DOI: [10.1103/PhysRevB.108.085117](https://doi.org/10.1103/PhysRevB.108.085117). URL: <https://link.aps.org/doi/10.1103/PhysRevB.108.085117>.
- [39] A. Stern and L. Fu, “Transport properties of a half-filled chern band at the electron and composite fermion phases,” *Phys. Rev. B*, Nov. 2023. DOI: [10.48550/arXiv.2311.16761](https://doi.org/10.48550/arXiv.2311.16761). URL: <https://doi.org/10.48550/arXiv.2311.16761>.
- [40] N. Paul, Y. Zhang, and L. Fu, “Giant proximity exchange and flat chern band in 2d magnet-semiconductor heterostructures,” *Science Advances*, vol. 9, no. 8, eabn1401, 2023. DOI: [10.1126/sciadv.abn1401](https://doi.org/10.1126/sciadv.abn1401). URL: <https://www.science.org/doi/abs/10.1126/sciadv.abn1401>.

- [41] P. Streda, “Theory of quantised Hall conductivity in two dimensions,” *Journal of Physics C Solid State Physics*, vol. 15, no. 22, pp. L717–L721, Aug. 1982. DOI: [10.1088/0022-3719/15/22/005](https://doi.org/10.1088/0022-3719/15/22/005).
- [42] G. H. Wannier, “A result not dependent on rationality for bloch electrons in a magnetic field,” *physica status solidi (b)*, vol. 88, no. 2, pp. 757–765, 1978. DOI: <https://doi.org/10.1002/pssb.2220880243>. URL: <https://onlinelibrary.wiley.com/doi/abs/10.1002/pssb.2220880243>.
- [43] G. Murthy and R. Shankar, “Hamiltonian theories of the fractional quantum hall effect,” *Rev. Mod. Phys.*, vol. 75, pp. 1101–1158, 4 Oct. 2003. DOI: [10.1103/RevModPhys.75.1101](https://doi.org/10.1103/RevModPhys.75.1101). URL: <https://link.aps.org/doi/10.1103/RevModPhys.75.1101>.
- [44] R. L. Willett, “Experimental evidence for composite fermions,” *Advances in Physics*, vol. 46, no. 5, pp. 447–544, 1997. DOI: [10.1080/00018739700101528](https://doi.org/10.1080/00018739700101528). eprint: <https://doi.org/10.1080/00018739700101528>. URL: <https://doi.org/10.1080/00018739700101528>.
- [45] V. Crépel and L. Fu, “Anomalous hall metal and fractional chern insulator in twisted transition metal dichalcogenides,” *Phys. Rev. B*, vol. 107, p. L201109, 20 May 2023. DOI: [10.1103/PhysRevB.107.L201109](https://doi.org/10.1103/PhysRevB.107.L201109). URL: <https://link.aps.org/doi/10.1103/PhysRevB.107.L201109>.
- [46] N. Morales-Durán, J. Wang, G. R. Schleder, M. Angeli, Z. Zhu, E. Kaxiras, C. Repellin, and J. Cano, “Pressure-enhanced fractional chern insulators along a magic line in moiré transition metal dichalcogenides,” *Phys. Rev. Res.*, vol. 5, p. L032022, 3 Aug. 2023. DOI: [10.1103/PhysRevResearch.5.L032022](https://doi.org/10.1103/PhysRevResearch.5.L032022). URL: <https://link.aps.org/doi/10.1103/PhysRevResearch.5.L032022>.
- [47] C. Wang, X.-W. Zhang, X. Liu, Y. He, X. Xu, Y. Ran, T. Cao, and D. Xiao, “Fractional chern insulator in twisted bilayer MoTe<sub>2</sub>,” *Phys. Rev. Lett.*, vol. 132, p. 036501, 3 Jan. 2024. DOI: [10.1103/PhysRevLett.132.036501](https://doi.org/10.1103/PhysRevLett.132.036501). URL: <https://link.aps.org/doi/10.1103/PhysRevLett.132.036501>.

- [48] B. I. Halperin, P. A. Lee, and N. Read, “Theory of the half-filled landau level,” *Phys. Rev. B*, vol. 47, pp. 7312–7343, 12 Mar. 1993. DOI: [10.1103/PhysRevB.47.7312](https://doi.org/10.1103/PhysRevB.47.7312). URL: <https://link.aps.org/doi/10.1103/PhysRevB.47.7312>.